



Stockholm
University



AKADEMISKA
SJUKHUSET

Investigation of dosimetric effects of radiopaque fiducial markers for use in proton beam therapy with film measurements and Monte Carlo simulations

Zerrin Uludag

Thesis for Master of Science in Medical Radiation Physics

2014-04-10

Supervisors:

Anders Montelius and Shirin Enger

ACKNOWLEDGMENTS

I would like to express my sincere gratitude to Professor Anders Ahnesjö for helpful advice.

ABSTRACT

Purpose: To estimate the dose perturbation introduced by implanted radiopaque fiducial markers in proton beam therapy (PBT) depending on the shape, orientation and localization of the marker. The aim was also to make a comparative study between the cylindrical proton gold marker (0.6 mm x 4.0 mm), used today in PBT, the photon marker (1.2 mm x 3.0 mm) and the Gold Anchor marker (0.28 mm x 20.0mm), a new type of marker developed by Naslund Medical AB for use in soft tissue.

Background: In radiation therapy (RT), fiducial markers are often used in order to facilitate the tumour localization by using image guided radiation therapy (IGRT). However, the use of x-ray opaque markers in PBT can introduce unacceptable underdosage behind the marker in the target resulting in less effective tumour cell kill.

Materials and methods: Radiochromic film measurements and Monte Carlo (MC) calculations based on the Geant4 general-purpose simulation toolkit were used in this work for the estimation of the dose perturbation in presence of fiducial gold markers. The experiments were performed at The Svedberg Laboratory (TSL) which offers proton beams with a passive scattering technique. The fiducials were imbedded into Blue wax and the films were stacked behind the wax between thin PMMA slabs. The experiments were carried out for fiducial markers positioned at the center and near the distal end of the spread out Bragg peak (SOBP). One of the experimental cases was simulated with MC (Geant4) where the dose perturbation was calculated in presence of the proton marker, oriented perpendicularly to the beam axis near the distal end of the SOBP.

Results: The radiochromic film measurements showed that all investigated markers reduced the target dose in small volumes. Target underdosage was largest for markers oriented parallel to the beam axis and localized at end of the SOBP. The proton marker, presently used at TSL, showed an underdosage at mid-SOBP of $12\pm 2\%$ and $22\pm 2\%$ for perpendicular and parallel orientations respectively. For the same position, the maximum dose shadows for the Gold Anchor were $4\pm 2\%$ and $19\pm 2\%$. For the proton marker oriented perpendicularly to the beam axis near the end of the SOBP the maximum dose perturbation measured with film was $21\pm 2\%$ compared to $19\pm 3\%$ obtained with MC. The observed underdosage with both methods agreed within their respective uncertainties.

Conclusion: The magnitude of the perturbation depends on the shape, thickness, orientation and localization of the markers. The effect was most pronounced for markers oriented parallel to the beam axis and increased with depth within the SOBP. As the perturbation increases with the thickness of the marker, the Gold Anchor marker gives less dose perturbation and may be used in future PBT.

ABBREVIATIONS

ADC- Analog to Digital Converter

BERT – Bertini Cascade

BG – Bragg Gray

BIC – Binary Cascade

BIC_Ion – Binary Light Ion Cascade

CBCT – Cone Beam Computed Tomography

CHIPS – Chiral Invariant Phase Space

CPU – Central Processing Unit

CT – Computed Tomography

CTV – Clinical Target Volume

EBT- External Beam Therapy

FORTTRAN – FORMulaTRANslation

FTFP – Fritop + Precompound

GEANT4 – Geometry And TRacking version 4

GTV – Gross Target Volume

IGRT – Image Guided Radiation Therapy

IMPT – Intensity Modulated Proton beam Therapy

ISP - International Specialty Products

LHEP - Low- High Energy Parameterized

MC – Monte Carlo

MCS – Multiple Coulomb Scattering

NIST – National Institute of Standards and Technology

n-type – negative charge type

OD – Optical Density

PBT – Proton Beam Therapy

PRECO – PRECOmpound

p-type – positive charge type

p-Si – p-type Silicon

PTV – Planning Target Volume

QBBC - Quark Gluon String + Bertini + Binary Cascade

QGSP - Quark Gluon String + Precompound

RGB – Red Green Blue

RM – Range Modulation

RT – Radiation Therapy

SAD – Source to Axis Distance

SOBP – Spread Out Bragg Peak

SSD – Source to Skin Distance

TSL – The Svedberg Laboratory

t_w – Water equivalent thickness

CONTENTS

1. INTRODUCTION.....	- 9 -
1.1 Proton interactions with matter.....	- 10 -
1.2 Proton Therapy	- 11 -
1.2.1 History.....	- 11 -
1.2.2 Beam Delivery	- 11 -
1.2.3 Dose perturbations due to inhomogeneities	- 13 -
1.3 Radiopaque fiducial markers for IGRT and PBT	- 14 -
1.4 Film Dosimetry.....	- 15 -
1.4.1 Radiochromic EBT film.....	- 15 -
1.4.2 Film readout with flatbed scanner.....	- 16 -
1.5 Semiconductor dosimetry	- 16 -
1.6 Geant4.....	- 16 -
1.6.1 Overview	- 16 -
1.6.2 Physics lists in Geant4	- 18 -
2. MATERIALS AND METHODS.....	- 20 -
2.1 Description of TSL beam line	- 20 -
2.2 Description of MC model	- 21 -
2.2.1 Geometry Definition	- 21 -
2.2.2 Generation of primary events.....	- 22 -
2.2.3 Cut off range	- 22 -
2.3 Adjustment of the Geant4 parameters and comparison with experimental measurements	- 22 -
2.4 The impact of the initial beam size and initial angular beam spread	- 23 -
2.5 EBT3 film measurements	- 24 -
2.5.1 Fiducial Markers used in this work.....	- 25 -
2.5.2 Position of fiducial markers in SOBP	- 25 -
2.5.3 Film Calibration	- 27 -
2.5.4 EBT3 measurements of the perturbed dose distribution.....	- 27 -
2.6 Geant4 estimation of the dose perturbation	- 29 -
2.7 Uncertainty analysis	- 30 -
2.7.1 Uncertainty in Monte Carlo calculations	- 30 -

2.7.2 Uncertainty analysis in EBT3 film measurements.....	- 30 -
3. RESULTS.....	- 31 -
3.1 Adjustment of the Geant4 parameters and comparison with experimental measurements	- 31 -
3.2 The impact of the initial beam size and initial angular beam spread	- 32 -
3.2 EBT3 film measurements	- 33 -
3.3.1 Film Calibration	- 33 -
3.3.2 Perturbed dose distributions.....	- 34 -
3.3 Geant4 estimation of the disturbed dose distribution	- 42 -
3.4 Comparison of experimental data with MC-calculations	- 43 -
4. DISCUSSION	- 45 -
4.1 Adjustment of the Geant4 dose distribution and comparison with experimental diode measurements	- 45 -
4.2 Estimation of the impact of the initial beam size and initial spread.....	- 45 -
4.3 EBT3 film measurements	- 45 -
4.4 Comparison of experimental data with MC-calculations	- 46 -
5. CONCLUSION.....	- 47 -
6. REFERENCES	- 48 -

1. INTRODUCTION

Every year nearly 13 million cases of cancer are diagnosed worldwide causing more than 7 million deaths [1]. The number of cancers is increasing but at the same time the survival rate increases due to better treatment and earlier detection. Today, cancer patients receive treatments with surgery, chemotherapy, radiation therapy and other forms of therapy. Radiation therapy (RT) is one of the most important modalities for local treatment of cancer and is given to about half of all cancer patients during the course of their treatment [2]. In Sweden about 25 000 patients receive RT every year and 99 % of them are treated with photons and electrons, usually called conventional RT [3,4]. The aim of RT is to kill all cancer cells with ionizing radiation while sparing healthy tissues. Proton beam therapy (PBT) is a type of RT which has been in clinical use for almost 60 years but it is only during the last decades that the number of proton beam facilities has increased markedly. Proton therapy in Uppsala started already in 1957 at the Gustaf Werner Institute and continues at the present The Svedberg Laboratory (TSL). The first dedicated proton beam centre in Scandinavia, the Skandion Clinic, is opening 2015 in Uppsala. Today around 40 proton facilities are in operation and a similar number are proposed or under development [4,5]. Proton therapy gives in comparison with photons equal or better tumour coverage and minimizes the irradiation of healthy tissues. The proton beam offers a biological effective dose which is close to the conventional beams too [6]. The properties of the proton beams make them attractive for radiation therapy but major drawbacks are the sensitivity to anatomical inhomogeneities and motion during treatment.

The techniques for delivering external beam radiation to the target have improved dramatically in the past decades. Today, the beam delivery to the target is more accurate, mainly due to improvements in beam shaping and improvements in aligning the beam to the target [7]. The accurate beam delivery is also facilitated by using opaque fiducial markers. The markers, typically three or four, are placed inside or near the target and by using x-ray imaging to position the patient, so called image guided radiation therapy (IGRT), the uncertainties in target location can be minimized.

Fiducial markers are often made of high density materials such as gold in order to be clearly visible with x-ray imaging. Depending on the treatment modality different markers are used. These markers can, however, cause artefacts on tomographic images and perturb the dose distributions of the therapy beams. Proton beams are much more sensitive to dose perturbation than photon beams. Today, cylindrical gold markers are often used both in photon and proton beam therapy. Newhauser et. al.,[7] reported that fiducial markers used in proton beam therapy cause a dose reduction which depends on the size, shape, density and position of the markers.

At the proton facility at TSL in Uppsala, titanium markers are used for intracranial treatments and small cylindrical gold markers are used for prostate treatments. A new type of marker, the Gold Anchor, has been developed by Naslund Medical AB for use in soft tissues. This type of marker is supposed to give less image artefacts and less dosimetric effects. The purpose of this study was to analyse the impact of the fiducial markers on the dose distribution in proton beams. Three markers, the Gold Anchor marker, the proton gold marker used at TSL and a gold marker used in photon beams were investigated. The dosimetric impact of the markers was investigated experimentally with Gafchromic EBT3 film measurements by positioning each marker at two different depths in the spread out Bragg peak (SOBP) region of the depth dose curve.

The experiments were performed at TSL which offers proton beams with a passive scattering technique. A Monte Carlo (MC) simulation with the Geant4 general-purpose simulation toolkit [8], version 9.05, was also performed for the investigation of the dose perturbation in presence of a proton marker

1.1 Proton interactions with matter

When protons travel through matter they lose energy and they slow down. The energy loss is mainly due to the Coulomb (electromagnetic) interactions between the protons and the orbital electrons of the matter which is also the main dose contributor. There are also small dose contributions from nuclear reactions [9], which also produce neutrons as a secondary radiation. The probability of nuclear reactions in PBT is around 1% per g cm^{-2} for a tissue-equivalent material and has threshold energy of around 20 MeV [15].

The rate of the energy loss per unit path length is known as stopping power. Hence, the mass stopping power is the rate of energy loss per unit path length divided by the density ρ of the matter. The mass stopping power for protons e.g. in water has its maximum at some hundred keV and is then decreased with increased energy. Thus, at the near end of the proton range, the energy of the protons decrease dramatically and the dose deposition increases. This means that maximum dose is deposited immediately before the maximum range resulting in a pronounced peak [10]. The peak is referred as the Bragg peak and the depth of the peak depends on the initial kinetic energy of the protons, and the matter composition [9].

When protons travel through matter, they undergo Coulomb interactions with the nuclei of the atom where the protons are deflected at very small angles [10]. The effect of a stack of proton deflections is known as Multiple Coulomb Scattering (MCS). The amount of MCS depends on the energy of the protons and the scattering material. For protons, the angular distribution from MCS is almost Gaussian in shape [9].

A proton beam coming from an accelerator is a narrow, nearly monoenergetic and monodirectional pencil beam. In order to cover an extended target laterally either passive scattering or active pencil beam scanning techniques are used. To cover the tumour extension in depth, the beam energy is modulated resulting in a spread out Bragg peak (SOBP, see Figure 1). Passive scattering and active pencil beam scanning techniques are discussed in more detail in section 1.2.2.

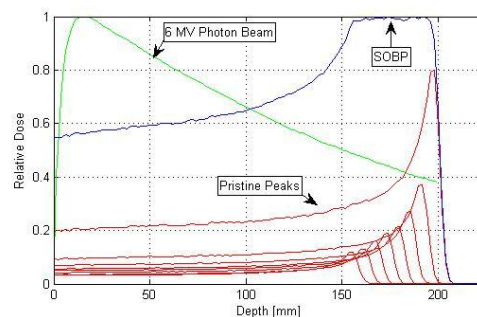


Figure 1: Proton depth dose curve in water where the modulated 180 MeV monoenergetic beam gives rise to the SOBP by adding the pristine peaks, discussed in section 1.2.2. The green curve illustrates a 6 MV photon beam for comparison.

1.2 Proton Therapy

1.2.1 History

In 1929, Ernest O Lawrence invented the cyclotron which at that time could accelerate the nuclear particles to a high velocity without using high voltage. This was the predecessor to the cyclotron used today. In 1946, Robert R Wilson, a student of Ernest O Lawrence, published a paper where he proposed medical treatment with cyclotron generated high energy proton beams [11]. Eight years later the first patient was treated at Berkeley Radiation Laboratory in California. In 1957, patients were treated successfully in Uppsala, Sweden at the Gustav Werner Institute (today The Svedberg Laboratory) [12].

Today, protons are accelerated to high energies by using cyclotrons or synchrotrons. For medical use, it is important that the accelerators are able to deliver high enough beam intensities and energies to treat all locations in the human body. This is achieved by using either passive scattering techniques or pencil beam scanning techniques [13,14].

1.2.2 Beam Delivery

Proton beams for RT can be delivered with two different techniques; passive scattering and active scanning. Passive scattering is to date the standard technique where scattering foils are used to laterally spread out the narrow beam from the accelerator to cover the target. The primary scattering foil with high atomic number broadens the proton beam into a Gaussian profile. To obtain a flat profile a secondary Gaussian shaped foil is used.

The monoenergetic beam is modulated by using a range modulator (RM) wheel or a ridge filter often mounted on a wobbling plate [9]. The RM wheel consists of a number of steps with specified thickness where each step corresponds to a specific pristine peak in the SOBP. The thickness of each step is adapted to the width of the pristine peak and the steps in the “stair case” of the RM-wheel which have angular widths are calculated to give a homogeneous depth dose over the SOBP [9]. There are a number of RM-wheels, each corresponding to an SOBP extension. At TSL, there are ten different RM wheels in use giving SOBPs ranging from 18 to 83 mm. Range compensators (bolus) are used to adapt the range of the beam to the shape of the target volume as illustrated in Fig 2.

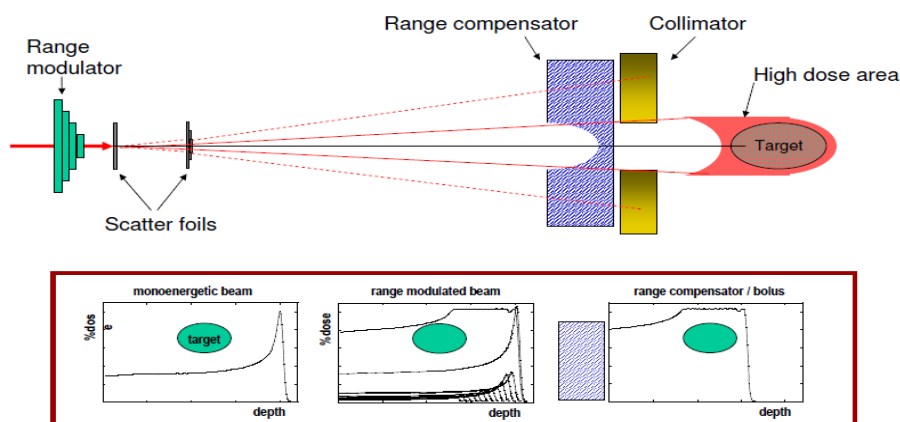


Figure 2: The dual foil technique provides lateral target coverage and the RM wheel enables target coverage in depth. The range can be adapted with range compensators in order to conform the dose to the target volume.

Proton therapy can also be delivered with pencil beam scanning techniques where the narrow pencil beam coming from the accelerator is scanned laterally by magnetic deflection [15], as it is illustrated in Figure 3. The modulation in depth is achieved by varying the energy of the pencil beam. Dose to the target is then delivered by scanning the Bragg peak of certain energy over the target. When the proton beam with the certain energy is delivered to the target, the beam energy is changed and the next layer is scanned. Layer after layer is scanned until the whole target volume is irradiated to the desired dose level. Active scanning has a number of advantages over the passive scattering techniques. One of the advantages is the possibility to use intensity modulated proton beam therapy (IMPT). IMPT can deliver dose with different scanning methods such as spot scanning and continuous scanning [15]. In spot scanning the dose is delivered in discrete spots while the pencil beam does not move and no dose is delivered during change in beam position. In continuous scanning (or raster scanning) the dose is delivered continuously during scanning, which requires the dose rate to be synchronised with the scanning speed.

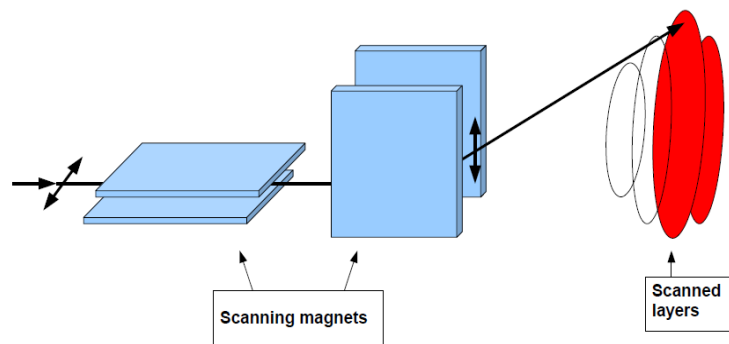


Figure 3: Active pencil beam scanning enables lateral target coverage by deflection with magnets. The modulation in depth is achieved by varying the energy of the pencil beam.

The major advantages of the beam scanning technique compared to passive scattering are better dose conformity, no beam specific modifiers and larger field sizes [15]. Furthermore, the production of neutrons is decreased in comparison with the use of passive scattering technique.

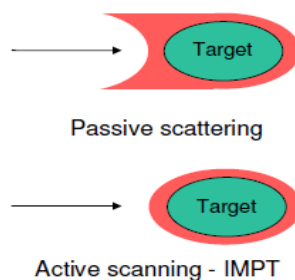


Figure 4: Active scanning enables a target dose coverage which can be tailored both at the distal and proximal end of the target.

One of the disadvantages with active scanning is the sensitivity to patient and organ movements [15]. Active scanning is an advanced method which requires a complex control system.

1.2.3 Dose perturbations due to inhomogeneities

Dose perturbations in PBT due to heterogeneities in the beam path are more critical for protons than photons. Inhomogeneities caused by differences in density and chemical composition e.g. between bone and tissue alter the penetration depth and the lateral scattering [15]. Fiducial markers introduce inhomogeneities that may cause dose perturbation. These perturbations may lead to cold and hot spots and can also affect the range of the beam. The influence of inhomogeneities will be discussed for three cases, illustrated in Figure 5.

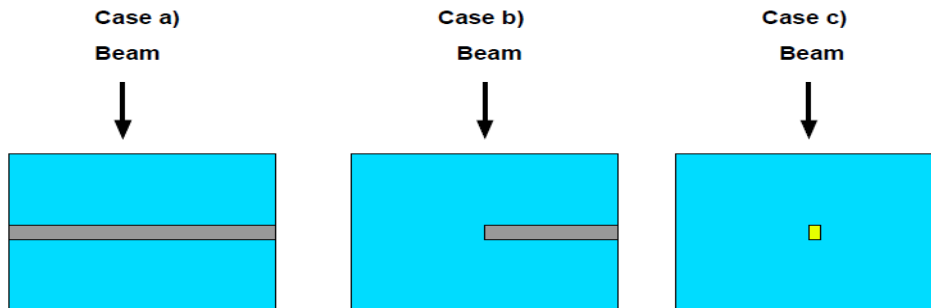


Figure 5: Three simplified cases where a) the uniform slab intersects the full beam, b) the uniform slab partially intersects the beam and c) a small complex inhomogeneity (gold marker) intersects the beam. (Adapted from [15])

As discussed in section 1.1 protons lose energy mainly through Coulomb interactions with orbital electrons and are deflected very little in each interaction with the nuclei of the atom. Fig 5, case a) illustrates a uniform slab which intersects the full proton beam. In this case, the energy fluence is virtually unchanged just after the inhomogeneity [15]. The beam range will, however, increase or decrease depending on the density of the slab.

In case b), where the slab partially intersects the beam, the beam penetration is altered in the shadow of the inhomogeneity. At the lateral boundary of the inhomogeneity, the differences in the density of the materials will result in differences in MCS of protons. Consequently, the differences in MCS will result in dose perturbation i.e. a cold spot on the high density side and a hot spot at the low density side [15]. If the complex inhomogeneity is localized near the end of the beam range the cold/and hot spot will be more pronounced due to the relatively low energy of the beam [16].

Case c) illustrates a gold marker which intersects with the beam. As in case b), the differences in the MCS will result in cold and hot spots. The dose perturbation depends on size, density, shape, orientation and localization of the marker. Newhauser et al., [16] showed that tantalum markers used in treatment of uveal melanoma in PBT reduced the target dose by 22-82%.

1.3 Radiopaque fiducial markers for IGRT and PBT

Image guided radiation therapy (IGRT) allows accurate localization of the tumour by imaging the patient's anatomy during or immediately prior to treatment. This means that the irradiated margins around the tumour can be reduced, which gives fewer complications.

Three different target definitions are generally used in treatment planning; gross tumour volume (GTV), clinical target volume (CTV) and planning target volume (PTV) [17]. The GTV is the tumour volume which can be seen, palpated or imaged and the CTV is the volume including the GTV plus margins for possible sub-clinical disease. The PTV margin around the CTV is taking into account all possible geometrical variations and inaccuracies in order to ensure that the prescribed dose is delivered to the CTV [17].

The information about the target localization obtained during or immediately prior to the course of the treatment can be used to correct for example the patient set-up errors. Patient set-up error is an interfraction uncertainty which occurs from fraction to fraction. On other hand, intrafraction uncertainty occurs during the irradiation of the target. This uncertainty is mainly due to internal organ movements such as patient breathing, heart beat or other internal movements [18]. IGRT is mainly applied to manage geometric set-up, but can in principle also be used to compensate for intrafraction uncertainties if imaging can be performed during treatment. In brief, IGRT enables a reduction of PTV margins and thus reduces dose to healthy surrounding organs without compromising the dose to the target [19].

In RT, the imaging can be performed with cone beam computed tomography (CBCT), kV- or MV x-ray imaging systems. The images taken at the time of treatment are compared with reference images created at treatment planning. The position is determined by aligning soft tissue structures, bony anatomy, fiducial markers or other landmarks [20]. Factors such as image quality, anatomical changes, and organ deformations determine how the alignment should be performed [20]. Radiopaque fiducial markers can be used as external surrogates to reproduce and increase the positioning accuracy of the target structures during RT [21]. These fiducial markers are placed inside or adjacent to the target volume.

Criteria for the markers are as follows [21,22];

- Visibility in the treatment planning and daily control images
- Causing few image artefacts
- Low dose perturbation
- No migration during treatment

Fiducial radiopaque markers are not perturbing the dose in photon beams as much as in proton beams, where high atomic numbers in the fiducial marker can give unacceptable dose perturbations. The shape and size of the marker is also crucial. The choice of fiducial marker depends on radiation type, the tumour location in the body and the chosen imaging system for IGRT etc.

For intracranial treatments titanium markers can be used and small cylindrical gold markers are often chosen for prostate treatments. Another choice is the new Gold Anchor marker developed by Naslund Medical AB for use in soft tissues.

The Gold Anchor marker can be folded in different ways depending on the tissue composition, the technique for the implantation and other factors. Figure 6 shows two examples of Gold Anchor used for IGRT in treatment of prostate cancer.

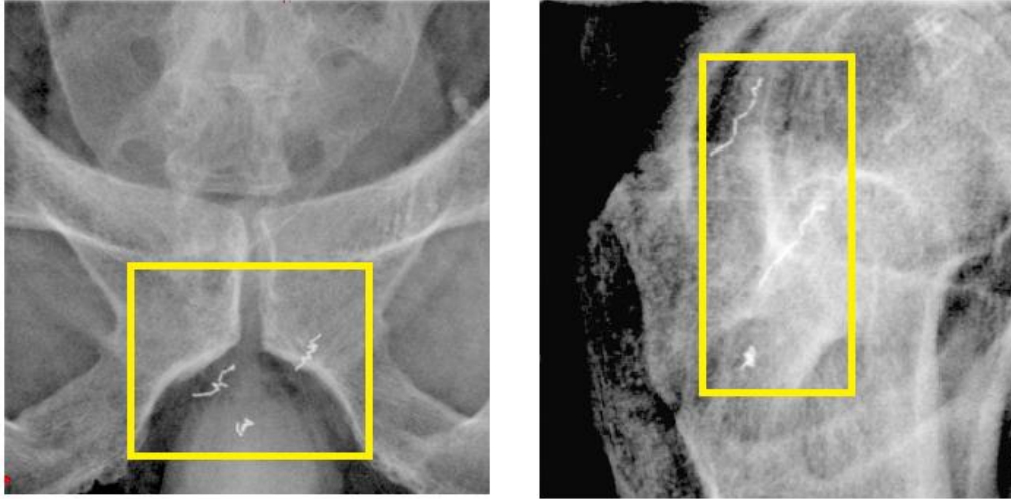


Figure 6: Examples on gold anchor markers in tissue, folded differently.

1.4 Film Dosimetry

In this work, dose perturbations from small fiducial markers were investigated with self-developing radiochromic films, Gafchromic EBT3 films, from International Special Products (ISP). The evaluation process was conducted with a flatbed scanner.

Film dosimetry offers an excellent two dimensional spatial dose resolution which enables detection of steep gradients in the dose distribution [23] e.g. in proton beam therapy. Each film has a thickness of 0.275 mm and by stacking a number of films it is possible to achieve good resolution also in three dimensions.

1.4.1 Radiochromic EBT film

Radiochromic films, based on poly-diacetylene have weak energy dependence in a broad energy range and are near tissue equivalent. In contrast to radiographic films, they are relatively insensitive to visible light and can be prepared under normal room light [24].

The radiochromic film, Gafchromic EBT film, is a relatively new film (released in 2004) which is an important tool in RT (e.g in dose verification) [25]. The film is optically transparent and gives a blue colour at exposure of radiation.. In addition, the film prevents also the formation of the Newton's Rings interference patterns in images [25] and has an excellent uniformity [26].

1.4.2 Film readout with flatbed scanner

Flatbed scanners have been used for a long time for radiochromic film readout. The flatbed scanner is a multichannel scanner i.e. the films can be scanned in red-green-blue (RGB) format. Moreover, an exposed Gafchromic EBT3 film has a strong absorbance in the red spectrum which makes the flatbed scanner useful tool [25].

Flatbed scanners such as EPSON Expression 1680 Pro allows scanning in transmission mode, i.e a uniform light source illuminates the film on one side and an imaging system is measuring the light transmission from many points on the sample simultaneously [27]. To achieve more accurate results it is important to scan all films in the same position and orientation [26].

1.5 Semiconductor dosimetry

The basic dose characterization of the proton beam was done using semiconductor dosimetry (Scanditronix p-Si diode). For depth dose and dose profile measurements semiconductors are of interest due to the good spatial resolution, high sensitivity and instant readout [23]. A semiconductor diode uses a p-n junction in the semiconductor material. The material is doped differently on either side of the junction which provides a voltage over the junction and radiation produced charges can be collected and measured [28]. This enables measurements without external bias voltage. One type of semiconductor diode is the Scanditronix p-Si dosimeter which is a p-n junction diode, used in the experiments, discussed in section 2.3.

1.6 Geant4

1.6.1 Overview

Geant4 is a flexible, object oriented MC toolkit written in C++ [29,30]. The toolkit consists of 17 major class categories as shown in Figure 7. In order to simulate in Geant4, the users has to implement her/his own Geant4 application by defining her/his own classes. There are three mandatory classes where the user describes the experimental set-up, the radiation field with its particles, and the physical models or processes in order to configure the simulation [29]. Additional optional classes such as event action, run action and tracking action can be added to the simulation. Figure 8 illustrates an overview of Geant4 simulation.

Geant4 provides geometry description and navigation, tracking and interaction of particles through matter with a choice of physical interaction models, visualization and user interfaces [8]. The geometry package in Geant4 provides the ability to describe a geometrical structure and propagate particles through it. Geometry modelling is based on a mother–daughter concept. Volumes are created by describing their shapes and physical characteristics and are placed inside their mother volumes in a hierarchical manner. As such, the larger volume, the mother volume, contains with some margin all other daughter volumes in the detector geometry. The coordinate system used to specify where the daughter volume is placed is the coordinate system of the mother volume. At the top of the hierarchy is the World Volume, outside of which no particle is tracked. Geant4 uses the concept of Logical Volume to describe the geometrical properties and physical characteristics associated to a geometry element such as its shape (solid), material, radiation detection behavior and whether a specific electromagnetic field is to be associated with it. Physical Volume is used to manage the spatial positioning of the Logical Volume. Different techniques can be used to place a Physical Volume. The user has the choice to place a Physical Volume once in its mother volume, or through parameterized placements position the same Logical Volume many times, resulting in

large savings in memory. Once the geometry has been built the simulation tracks each particle through the geometry. Geometrical tasks such as determining the next traversed volume and obtaining distance to this volume are handled by ‘Navigator’ classes. Geant4 includes several different navigators, some appropriate for any volume arrangement; others designed specifically for optimal performance in simple voxel geometries [31]. Parallel Geometries are also available in Geant4, allowing the user to define additional geometrical hierarchies that overlay the standard World Volume which contains mass [8,32]. While these parallel worlds have no mass (and thus do not affect the fundamental physics processes), they are still seen by all navigators. Boundaries seen in this parallel geometry can be used to control other aspects of the simulation such as geometrical event biasing or scoring.

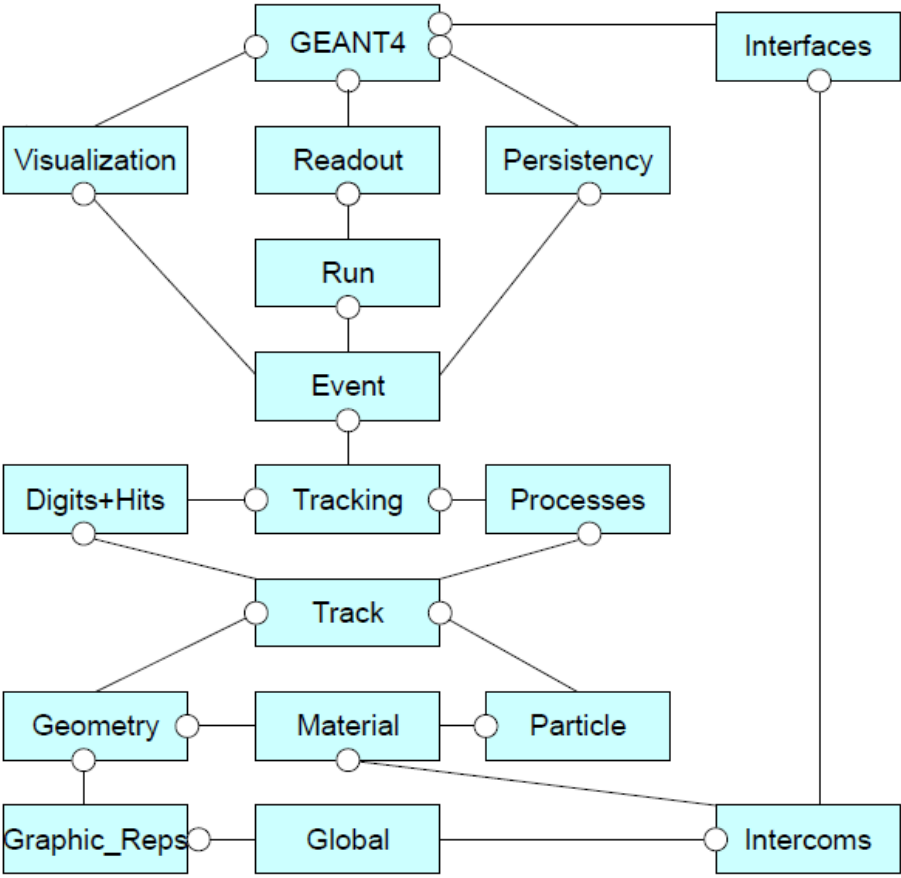


Figure 7: Geant4 class categories. (Adapted from [33])

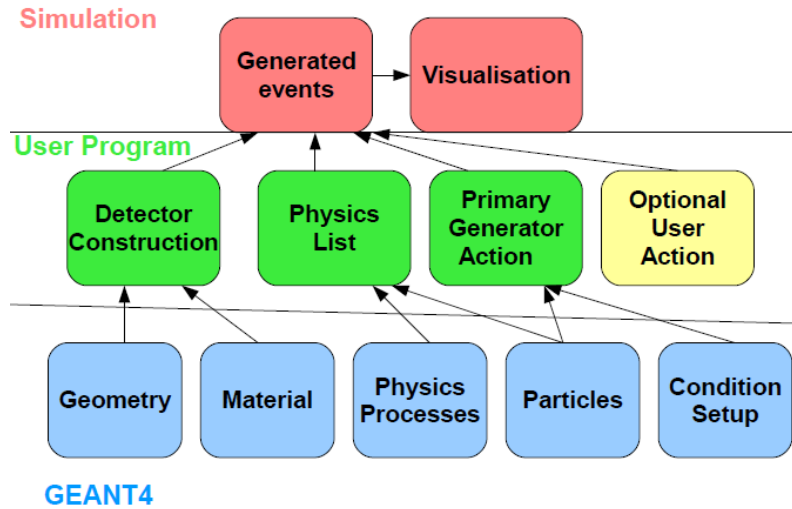


Figure 8: An overview of Geant4 simulation where the green boxes represent the mandatory classes. (Adapted from [34])

1.6.2 Physics lists in Geant4

Geant4 provides reference physics lists for the simulation of electromagnetic and hadronic interactions. There are different physics lists which can be used depending on the case. Each physics list is applying models for different energy ranges. The string model is commonly used for energies between 5 and 25 GeV. For lower energies, intranuclear cascade models or precompound models are used [35]. An overview at some provided hadron models can be seen in table 1.

Table 1: Some physics lists provided from Geant4. (Adapted from [36])

Models	Energy range	Particles
LHEP (Low- High Energy Parameterized)	0-100 TeV	All hadrons
PRECO (Precompound)	0-100 MeV	Protons and neutrons
BERT (Bertini Cascade)	0-15 GeV	Protons,neutrons,pions, kaons,hyperons
BIC (Binary Cascade)	0-5 GeV	Protons,neutrons,pions
BIC_Ion (BinaryLightIon Cascade)	0-5 GeV/u	Ions
QGSP (Quark Gluon String + PRECO)	10-10 ⁵ GeV	Protons,neutrons,pions and kaons
FTFP (Fritiof + PRECO)	3-10 ⁵ GeV	Protons,neutrons,pions, kaons and hyperons
CHIPS (Chiral Invariant Phase Space)	0-100 TeV	All hadrons

A detailed description of the physics models can be read in the Geant4 reference manual [37]. A brief description of the relevant physics lists is given below, quoted from [35].

QGSP – “QGSP is the basic physics list applying the quark gluon string model for high energy interactions of protons, neutrons, pions, and Kaons and nuclei. The high energy interaction creates an excited nucleus, which is passed to the precompound model modelling the nuclear de-excitation.”

QGSP_BERT – “Like QGSP, but using Geant4 Bertini cascade for primary protons, neutrons, pions and Kaons below ~ 10 GeV. In comparison to experimental data we find improved agreement to data compared to QGSP which uses the low energy parameterised (LEP) model for all particles at these energies. The Bertini model produces more secondary neutrons and protons than the LEP model, yielding a better agreement to experimental data.”

QGSP_BIC - “Like QGSP, but using Geant4 Binary cascade for primary protons and neutrons with energies below ~ 10 GeV, thus replacing the use of the LEP model for protons and neutrons. In comparison to the LEP model, Binary cascade better describes production of secondary particles produced in interactions of protons and neutrons with nuclei.”

Ivantchenko et. al. [36] reports that the Binary cascade model shows better result for low energy protons and neutrons and the Bertini cascade model is better for the remaining particle types. Therefore a new physics list, QBBC, has been created which includes combinations of BIC, BIC-ION, BERT, CHIPS, QGSP and FTFP models. In comparison, QBBC has higher precision for many hadron-ion and ion-ion interactions in a wide energy range.

QBBC uses the same inelastic cross-sections as QGSP_BERT for almost all hadrons and the final state depends on the energy of the particle. The BIC model, followed by Precompound and de-excitation, is used below 1.5 GeV, BERT is used from 1-5 GeV, FTFP is used from 4 to 25 GeV and QGSP is used above 12.5 GeV [38].

2. MATERIALS AND METHODS

The magnitude of the dose perturbation in PBT in presence of fiducial gold markers was investigated depending on the markers shape, implantation depth and orientation. The investigation was carried out through an experimental study and an MC simulation. The MC calculation was performed for one of the experimental situations where the proton marker, oriented perpendicularly to the beam axis, was positioned near the distal end of the SOBP.

The examination included also an adjustment of the Geant4 dose distributions and comparisons with the experimental dose measurements. Moreover, the initial beam spread in water was also investigated by varying the initial Gaussian beam size and angular width, discussed in section 2.3 and 2.4.

All data were obtained in form of ASCII files which were analysed in MatLab R2011b.

2.1 Description of TSL beam line

The experiments were performed with a therapy beam using passive beam scattering technique at The Svedberg Laboratory (TSL) in Uppsala. The facility is using the Gustaf Werner cyclotron, which produces proton beams with energy of 180 MeV. The proton beam, after passing through a vacuum window, scattering foils and air degraded is to 172 MeV.

The beam irradiation system at TSL consists of a primary lead foil, secondary Gaussian shaped gold foil, an aluminium foil supporting the gold foil, a range modulator, transmission ion chambers and collimators which can be seen in Figure 9.

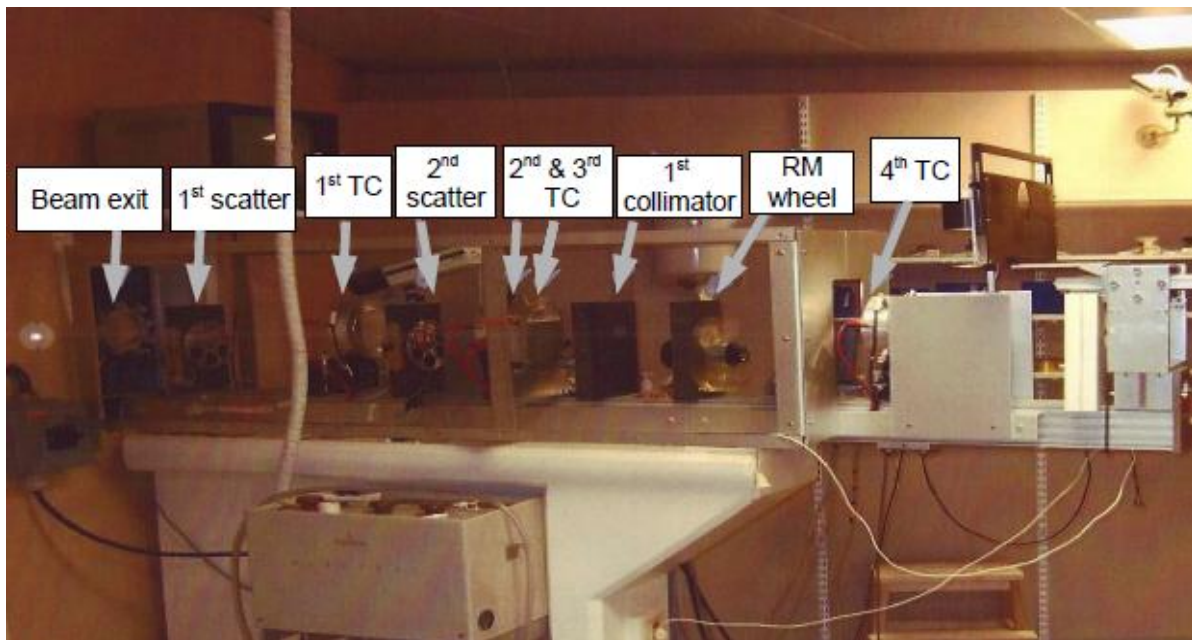


Figure 9: The TSL beam path consisting of the scattering system, range modulator, transmission ion chambers (TC) and collimators.

2.2 Description of MC model

Calculations were carried out using the Geant4 Monte Carlo code, release version 9.05. The code was run on a MAC computer (Apple Inc) at the Uppsala University Hospital.

2.2.1 Geometry Definition

The simulation of the experimental setup defined in Geant4 had the following geometrical properties:

- Primary lead foil with a thickness of $10.25 \text{ cm}^2/\text{g}$
- Secondary Gaussian shaped gold foil with a maximum thickness of $0.55 \text{ cm}^2/\text{g}$
- An aluminium foil supporting the gold foil with a thickness of $0.053 \text{ cm}^2/\text{g}$
- Circular brass collimator with apertures of 40 mm or 70 mm
- Voxelized water/PMMA phantom ($150 \times 150 \times 230 \text{ mm}^3$), using the parallel world concept and nested parameterization, where the dose deposition was scored in the voxels

TSL beam path components such as transmission ionization chamber and other collimators with little effect on the beam path were not defined in the MC application.

The shape of the secondary gold foil was determined with calculated data from Fig 10 [39].

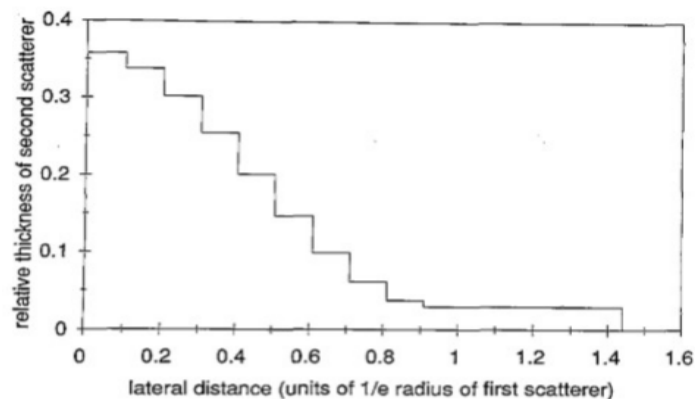


Figure 10: The curve which was used to obtain the thickness of each layer for the secondary Gaussian shaped gold foil. (Image taken from [39])

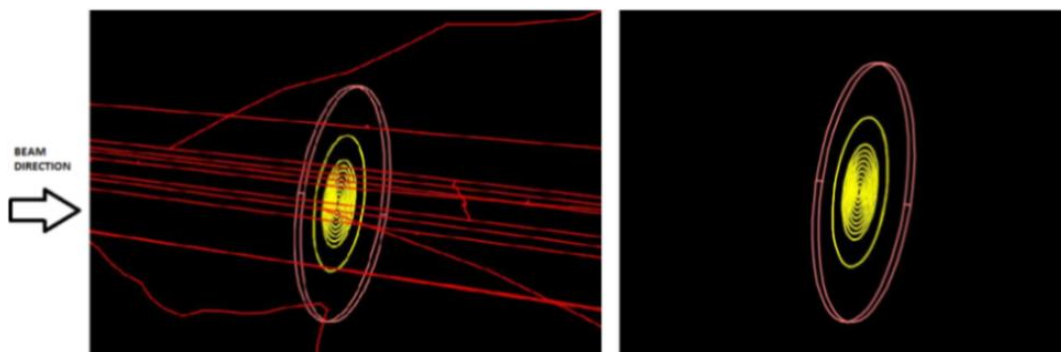


Figure 11: Secondary gold foil and the supporting aluminium foil in Geant4. The red tracks show typical proton paths.

2.2.2 Generation of primary events

The unmodulated, nearly monoenergetic Gaussian shaped proton beam had a beam radius of 0.625 mm at three standard deviations and an angular beam width of 0.001 radians at FWHM with energy of 178.3 ± 0.2 MeV. The SOBP was created by adding eight beams with different energies and weights providing a 48 mm deep SOBP.

2.2.3 Cut off range

The physics list QBBC was used for all simulations. For the simulations, the parameter production cut was used. Geant4 offers the user to define the production cuts in terms of range which is thereby converted into cut off energy. The cut off range should be defined to 1/3 of the voxel size [40]. In the simulations, cut off ranges for protons, electrons and positrons were determined depending on the investigated case. Since, the main dose deposition is due to the protons, electrons and positrons, secondary particles such as gammas and neutrons had a cut off range of 1000 mm in all simulations, which means that they were neglected in the calculation.

2.3 Adjustment of the Geant4 parameters and comparison with experimental measurements

The MC calculations were benchmarked with experiments in the proton beam made with semiconductor detectors. This gives more accurate results as MC beam parameters can be adjusted to the measured depth dose distributions. The MC range of the monoenergetic proton beam was adjusted to the experimental curve by changing the initial energy of MC. The adjustment was performed for the nearly monoenergetic uncollimated proton beam. Thereafter, a comparison between the obtained dose distributions from the diode measurement and the simulations were performed. The Scanditronix p-Si diode was used which has a spatial resolution of 0.05 mm along the beam axis and 2 mm laterally.

Following comparisons were performed;

1. Comparison of the uncollimated, nearly monoenergetic proton beam depth dose curve in water
2. Comparison of the uncollimated lateral dose profiles for unmodulated proton beam at 100 mm and 160 mm depth in water
3. Comparison of range modulated SOBP depth dose distribution in water

Figure 12 illustrates the MC beam line (a simulation of the experimental setup).

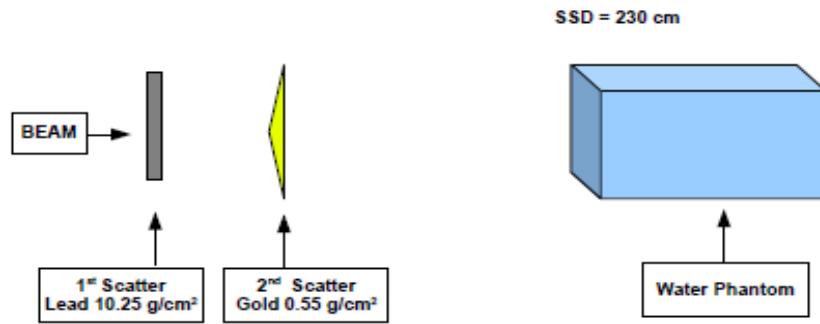


Figure 12: Illustration of the MC setup with a SSD of 230 cm. The water phantom used in the simulation had a voxel size of $5.0 \times 5.0 \times 2.0 \text{ mm}^3$ and the cut off range was 0.5 mm. 3 million protons were tracked with a step size of 0.01 mm for the unmodulated depth dose and dose profile comparisons and 50 million protons were tracked with a step size of 0.1 mm for the SOBP verification.

2.4 The impact of the initial beam size and initial angular beam spread

In order to obtain a uniformly distributed dose, the proton pencil beam is spread laterally with the passive scattering technique and extended in depth with the RM wheel. The shape of the beam, entering the water phantom is also depending on the initial beam size and initial angular beam spread.

The impact of initial beam size and initial angular beam spread was investigated in water for the nearly monoenergetic 180 MeV beam. The radial and angular Gaussian parameters for the initial beam were varied for the investigation in order to find the best fit with experiment, see table 2. The initial beam spread in water could be estimated by examining the penumbras of the dose profiles at 100 mm and 160 mm in water using a collimator with a diameter of 40 mm positioned 50 mm from the surface of the water phantom.

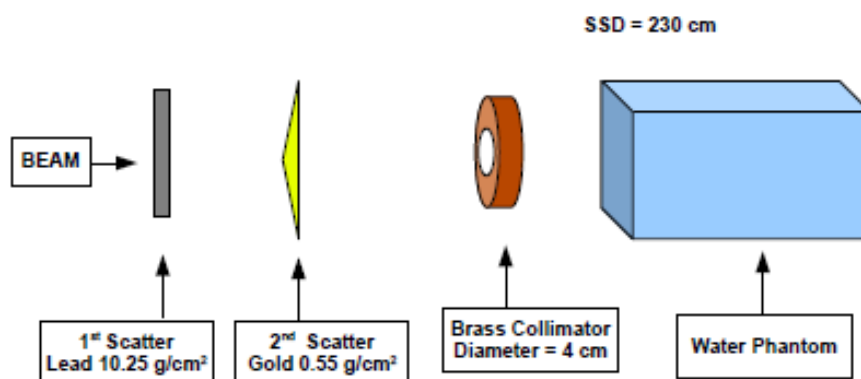


Figure 13: MC set-up for the monoenergetic lateral dose measurement in water. The water phantom had a voxel size of $2.0 \times 2.0 \times 5.0 \text{ mm}^3$ and the cut off range was 0.5 mm. The brass collimator used at the experiments with a diameter of 40 mm, 50 mm away from the surface of the water tank.

Table 2 shows the beam parameters for the investigation of the initial beam spread in water. The radial beam parameter corresponds to radius of the Gaussian beam with 3σ (standard deviations) and the angular beam parameter corresponds to the radius of the angular width of the Gaussian beam at FWHM. Note that when the initial beam angular width was varied, the radial beam parameters were fixed and vice versa.

Table 2: The radial and angular Gaussian beam parameters used in the MC simulation are shown in the table. In order to draw a conclusion about the initial spread in water was a collimator with an aperture of 4 cm used. For each simulation, 100 million protons were tracked with a step size of 0.1 mm.

	Radial beam parameters	Angular beam parameters
1st Simulation	0.625 mm	0 rad
2nd Simulation	0.625 mm	0.001 rad
3rd Simulation	0.625 mm	0.01 rad
4th Simulation	0.25 mm	0.001 rad
5th Simulation	1.5 mm	0.001 rad
6th Simulation	2.5 mm	0.001 rad

2.5 EBT3 film measurements

Dose perturbation in presence of fiducial markers in PBT was investigated with EBT3 film measurements. The scanner used to evaluate the films (Epson Expression 1680 Pro) offers a maximum resolution of 3200 dpi (dots per inch) which is extremely high. For the film readout process, a resolution of 150 dpi was used and the films were scanned in red channel mode (16 bit pixel depth) due to better response in the dose range used in the experiments.

The film experiments were performed in a multi-slab PMMA phantom where the markers were imbedded into a layer of Blue Wax (Freeman Manufacturing and Supply Company) which is mainly composed of polyethylene ($(-C_2H_4-)_n-$). The markers had to be placed in a nearly water equivalent material without air cavities and therefore Blue Wax was chosen as the markers could be placed in the desired orientation when the wax was heated to liquid phase. The surfaces of the solid wax slab were machined to fit into the PMMA phantom.

The beam was collimated to a circular diameter of 70 mm and the collimator was placed directly in front of the phantom. The range modulation width was 48 mm and the range of the beam in water was 197 mm to the distal 90% dose level as measured with the diode.

2.5.1 Fiducial Markers used in this work

Three different gold markers were investigated in this work. Their dimensions are shown in Table 3.

Table 3: Dimensions of the investigated radiopaque fiducial markers.

Fiducial marker	Length (mm)	Diameter (mm)
Gold Anchor	20.0	0.28
Proton marker	4.0	0.6
Photon marker	3.0	1.2

The Gold Anchor marker differed from the other gold markers, which consists of pure gold, by having a material composition of 99.5 % pure gold and 0.5 % iron and also by being flexible in the tissue. The marker has ten 2 mm long sections and the idea is that the curly marker will be “anchored” in the tissue and therefore keep its position.

The impact on the dose distribution from the Gold Anchor marker was examined for two shapes. In the first case, the marker was folded as a zigzag with an angle of 90° between the sections. In the second case, the Gold Anchor was curled into an irregular “ball”.

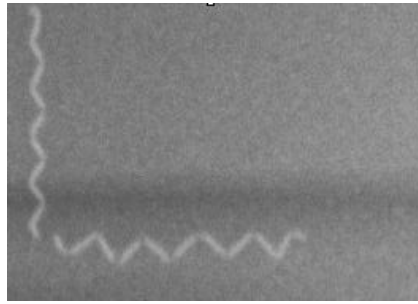


Figure 14: X-ray image of how the zigzag Gold anchor marker was oriented in the work.

2.5.2 Position of fiducial markers in SOBP

The dose perturbations were investigated for markers positioned at the middle and at the end of SOBP (see Figures 15, 16 and 17). The markers were oriented parallel and perpendicular to the direction of the incoming beam.

The radiological thickness of the materials used was expressed in terms of water-equivalent thickness (t_w) so that the markers could be positioned at the desired positions in the depth dose distribution. From the obtained SOBP curve in water from section 3.3.1, the corresponding t_w of PMMA used in the experiments could be calculated with equation (1) [7],

$$t_w = t_m(\rho_m/\rho_w) / (\overline{S_m}/\overline{S_w}) \quad (1)$$

where t_m is the thickness of the material, ρ_m and ρ_w is the density of the material and water, $\overline{S_m}$ and $\overline{S_w}$ are the corresponding mean proton mass stopping powers. In this work an average relative value of $t_w=1.16$ for the PMMA thickness [41] and $t_w=1.00$ for blue wax was used [42].

Table 4: Position of the downstream edge of the markers and associated reading errors at mid- and near the end of SOBP in terms of water-equivalent thickness.

Marker	Mid-position of the SOBP	Near end position of the SOBP
Proton marker	162.5±0.3 mm	186.4±0.3 mm
Zigzag Gold Anchor	161.6±0.3 mm	186.5±0.3 mm
Curled Gold Anchor	-	186.5±0.3 mm
Photon marker	-	185.8±0.3 mm

The figures below illustrate different positions and orientations of the markers at the middle and near the end of the SOBP.

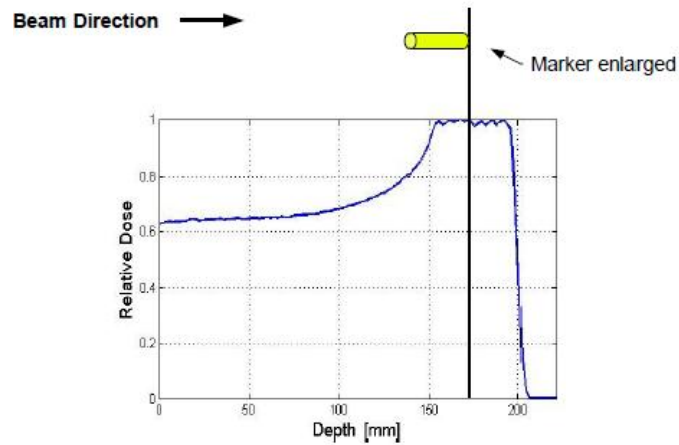


Figure 15: The proton marker (0.6 mm x 4.0 mm) positioned at the middle of SOBP parallel to beam axis.

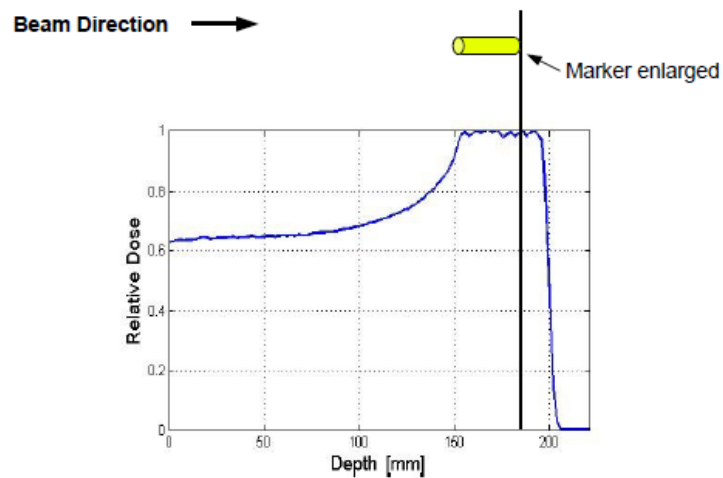


Figure 16: The proton marker (0.6 mm x 4.0 mm) positioned near the end of SOBP parallel to beam axis.

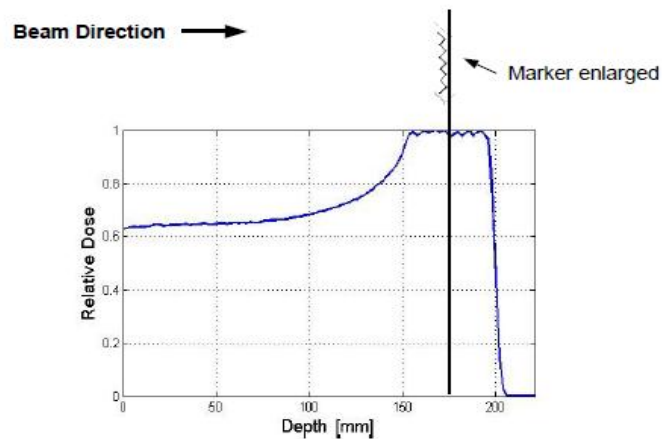


Figure 17: The zigzag Gold Anchor marker (0.28 mm x 20.0 mm) positioned at the middle of SOBP perpendicular to beam axis.

2.5.3 Film Calibration

A calibration was performed to convert the measured optical density of the EBT3 films to absorbed dose. To obtain the calibration curve the films were irradiated with doses of 1, 2, 3 and 4 Gy, which covered the dose range used in the experiments. The absorbed dose was determined with a calibrated ionization chamber according to IAEA TRS 398 [43].

The distance from the primary scattering foil to the film was 2300 mm. The films were placed behind 99 mm PMMA and 67 mm blue wax, which corresponds to approximately $t_w = 182$ mm. A 10 mm thick PMMA slab was placed behind the film to achieve full backscattering.

The exposed films were stored in a black envelope even though that the films were relatively insensitive to visible light. This was done in order to minimize the effect of uncertainties. The self-processing films were read out with the flatbed scanner 24 hours after the exposure. During the course of scanning, the film orientation was taken into account and the films were placed at the middle of the flatbed scanner. A correction for the background was done by subtracting readings from an unexposed film. The film reading and optical density-to-dose conversion was done with the software OmniPro I'mrt (IBA Dosimetry). The density-dose relationship was fitted by using third-order polynomials and the goodness of the fit could be determined by observing the residuals i.e the differences between the fit and the measured values.

2.5.4 EBT3 measurements of the perturbed dose distribution

The dosimetric effects of the fiducial markers were investigated by using a phantom comprised of PMMA slabs, Blue wax with the imbedded markers and a series of EBT3 films stacked between thin PMMA slabs.

When the markers were positioned at the middle of SOBP 16 films were stacked between PMMA slabs with an average thickness of 2 mm in order to cover a water equivalent depth range of >38 mm. For the markers positioned near the end of the SOBP, 10 films were stacked between PMMA slabs with an average thickness of 1 mm covering a water equivalent depth range of >12 mm. As for the mid-SOBP position the markers were positioned parallel and perpendicular to the incoming proton beam. Due to the varying thickness of the Blue wax slabs and the limited number of PMMA slabs, the positioning of the markers at SOBP was somewhat shifted from marker to marker.

The experimental setup is shown in Figure 18 and 19.

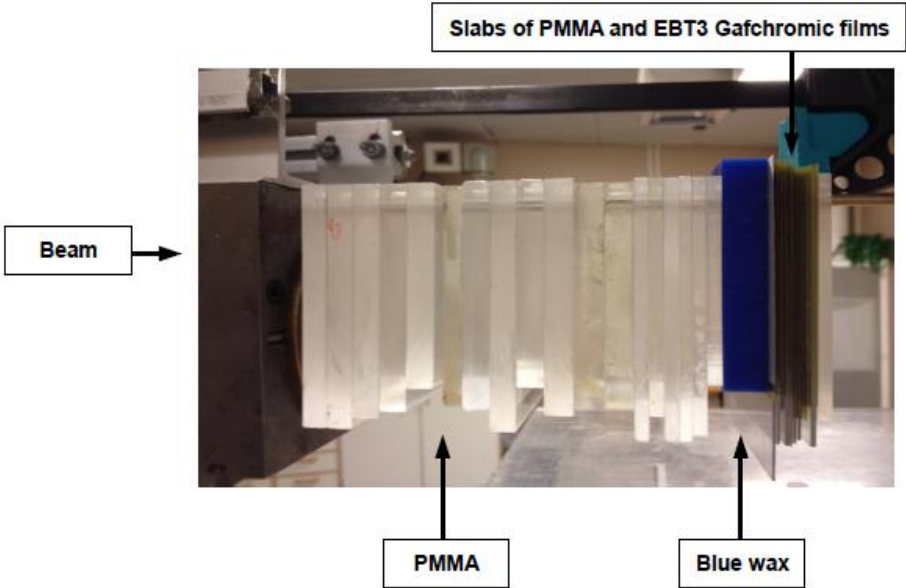


Figure 18: The phantom used in the experiments composed of PMMA slabs, Blue wax and EBT3 films.

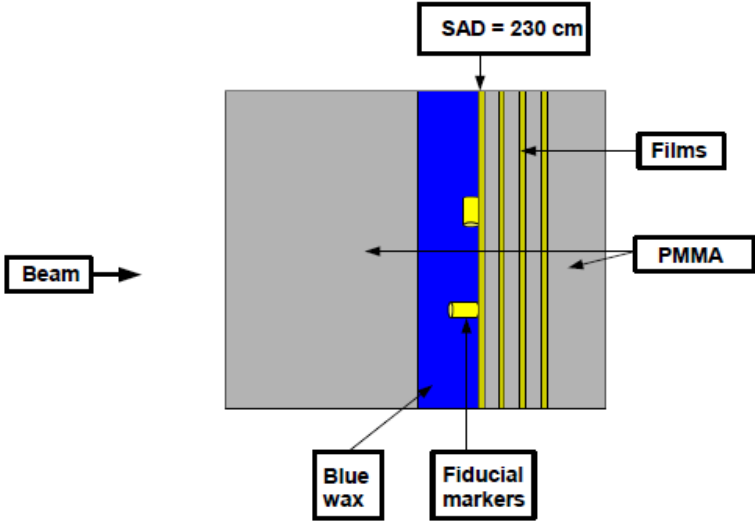


Figure 19: Schematic diagram (not to scale) showing the phantom with a series of EBT3 films stacked on the end of the downstream edge of the fiducial markers

The percentage perturbations introduced in presence of markers were determined by examination of the relative dose profiles obtained from the measurements. Fig 20 illustrates how the calculation of the dose reduction ($\% \Delta D_{\text{mean}}$) was performed. The mean value of the red region (the perturbed region) was divided by the mean value of the two black regions (unperturbed regions). Also the maximum dose reduction ($\% \Delta D_{\text{max}}$) in the corresponding dose profile was calculated relative to the mean value of the two black regions.

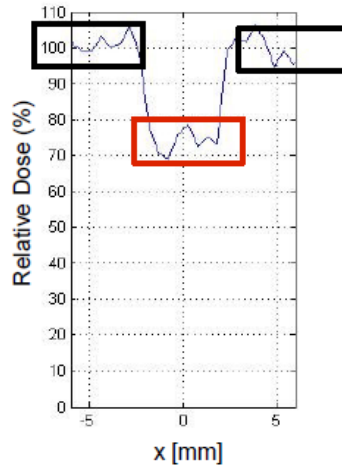


Figure 20: Relative dose profile illustrates the examination of the dose reduction in presence of a marker.

2.6 Geant4 estimation of the dose perturbation

The dose perturbation was calculated with Geant4 for one of the experimental situations where the cylindrical proton marker was located near the end of the SOBP and oriented perpendicular to the beam axis. The dose calculation was done in a PMMA phantom where each voxel was $0.5 \times 0.5 \times 1.0 \text{ mm}^3$.

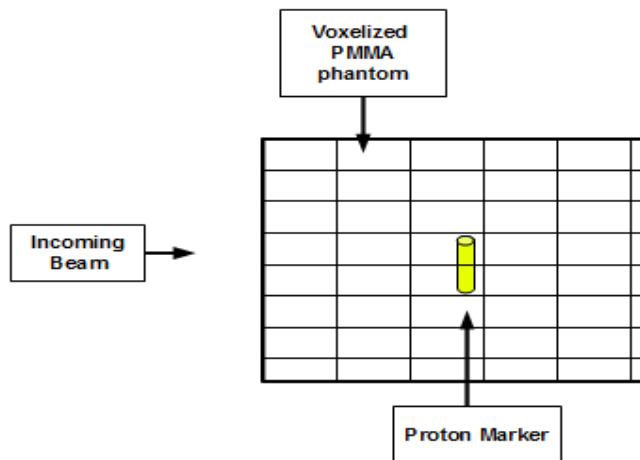


Figure 21: An illustration of the position of the proton marker in the voxelized PMMA phantom in the application. Note that in the experimental setup, the marker was placed in Blue wax.

For the calculation, 15 independent runs were performed in order to minimize the run time and also in order to estimate the statistical uncertainty, see section 3.7.1. Each run was consisting of 20 million primary protons. The cut off range was 0.15 mm and the step size was 0.01 mm.

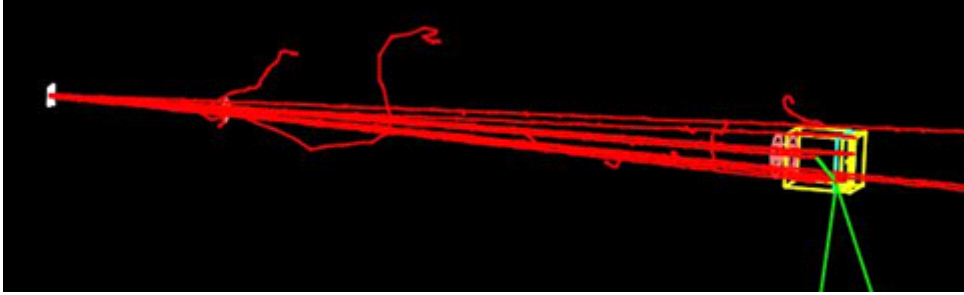


Figure22: The experimental set up in Geant4. The red tracks are travelling protons and the green tracks are gamma rays which in high probability were emitted during nuclear reactions.

The maximum percentage dose perturbation was determined by investigation of the MC calculated relative doses.

2.7 Uncertainty analysis

2.7.1 Uncertainty in Monte Carlo calculations

There are two methods to calculate the statistical uncertainties (type A) in MC. The first method is the batch method and the second one is the history-history method which requires data on dose per particle. In this work, the batch method was used due to limited data on each particle. The statistical uncertainty was calculated with equation (3),

$$s_{\bar{d}} = \sqrt{\frac{1}{n(n-1)} \sum_{i=1}^n (d_i - \bar{d})^2} \quad (3)$$

where n is the number of runs, d_i is the scored dose in a preselected undisturbed voxel in SOBP in run i , and \bar{d} is the mean value of the absorbed dose over the preselected voxels in all runs. As discussed in the previous section, 15 runs were simulated. Monte Carlo enables the user to estimate the statistical uncertainty.

2.7.2 Uncertainty analysis in EBT3 film measurements

An estimation of the type A uncertainty for the EBT3 film measurement was calculated using eq(4),

$$s_{\bar{D}} = \sqrt{\frac{1}{N(N-1)} \sum_{i=1}^N (D_i - \bar{D})^2} \quad (4)$$

where N is the number of films, D_i is the absorbed dose in the preselected pixel in film i , and \bar{D} is the mean value of all D_i . The statistical fluctuation was determined by using 4 films, used in the film measurements near the end of SOBP. D_i was corresponding to an undisturbed pixel in the central part of each film. All films were handled in the same way and were localized almost in same position at SOBP.

All type B uncertainties which couldn't be estimated were neglected in this work. The uncertainty introduced due to the calibration was also neglected due to very small uncertainties.

3. RESULTS

3.1 Adjustment of the Geant4 parameters and comparison with experimental measurements

Figures 23, 24 and 25 show the experimental dose distributions compared with Geant4 simulations described in section 3.3. In Fig 23 the calculated and measured depth dose distributions are shown. An initial energy of 178.3 ± 0.2 MeV in the MC simulation gave good agreement with experiment.

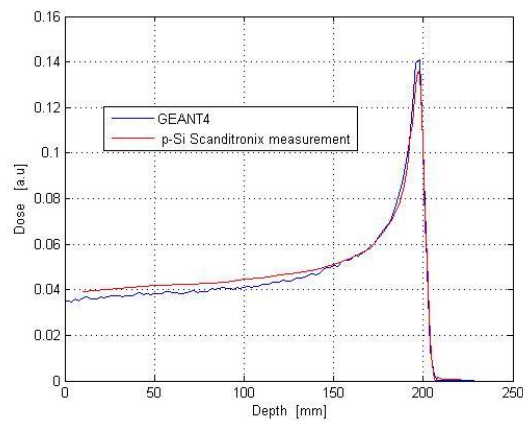


Figure 23: Unmodulated (nearly monoenergetic) proton depth dose curve (red curve) measured with semiconductor dosimetry and simulated Geant4 curve (blue curve) versus depth in water. The initial energy of the Geant4 beam was determined to 178.3 ± 0.2 MeV. Obtained data are normalized to the area under the curve.

In Fig 24 the calculated and measured lateral dose distributions are shown at depths of 100 mm and 160 mm in the water phantom. As can be seen in the figure there are some differences between the dose profiles especially at the edges. This is mainly explained with the differences between the experimental beam line and the simplified MC beam line. However, this is of less concern in the film measurements where the markers are located at the central part of the irradiation region with homogenous dose.

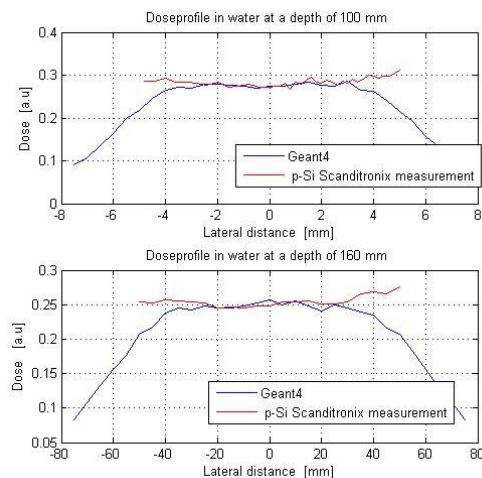


Figure 24: Dose profiles of the measured and simulated unmodulated and uncollimated proton beam at a) 100 mm and b) 160 mm versus the lateral distance in water. Obtained data are normalized to a region corresponding ± 25 mm in the lateral distance.

Fig 25 shows the measured and the MC calculated SOBP curve. Here is also a good agreement between the two curves where the modulation width is 48 mm.

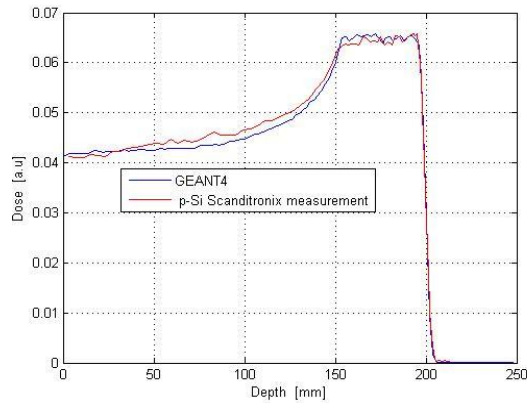


Figure 25: The diode measured modulated beam (red curve) and the weighted Geant4 beam (blue curve) versus depth in the water. Obtained data are normalized to the area under the curve.

3.2 The impact of the initial beam size and initial angular beam spread

The impact of the initial beam size and initial angular beam spread was investigated in water. The dose profiles at 100 mm and 160 mm were calculated with a brass collimator with an aperture of 40 mm for varying initial beam radius and angular width, see Fig 26 and 27. A comparison between the calculated penumbras and the experiment showed that the impact of initial beam size and initial angular spread has no effect on the resulting dose profiles in water. See also Discussion, section 4.

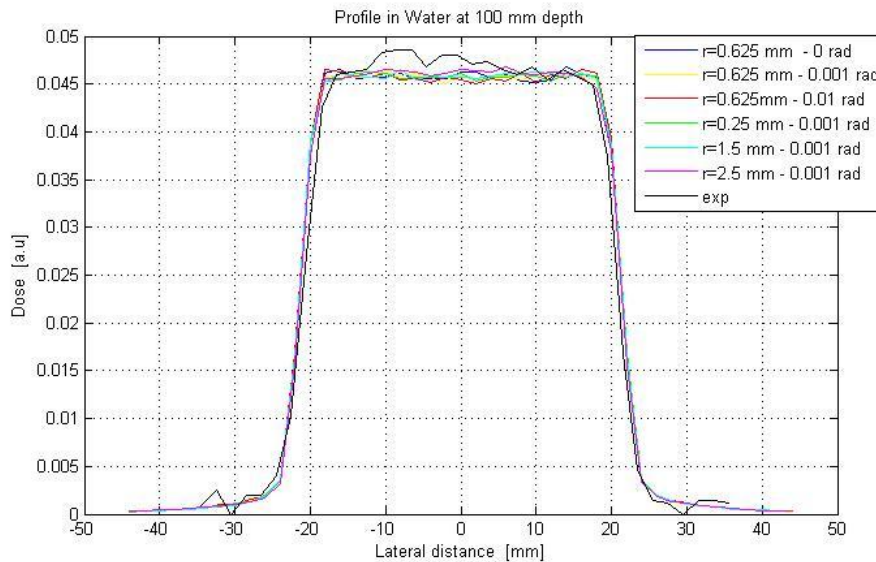


Figure 26: Dose profile at a depth of 100 mm obtained with Geant4 simulations and diode measurement. The investigation was carried out through varying beam radius r and the radius of the angular beam width. The black fit represents the experimental measurement. Obtained data were normalized to the area under the curve.

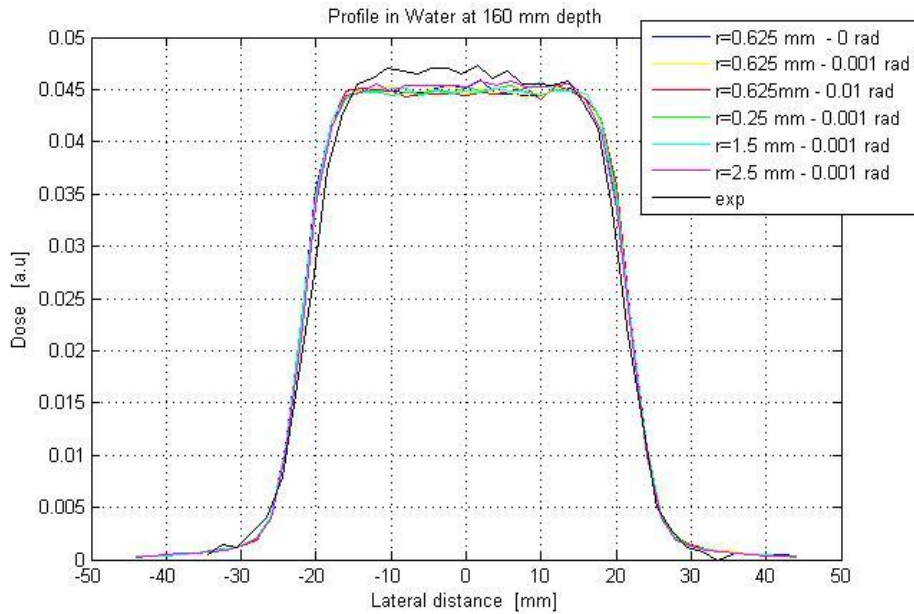


Figure 27: Dose profile at a depth of 160 mm obtained with Geant4 simulations and diode measurement for the investigation of the initial spread in water. The dose profiles correspond to different beam radius r and the radius of the angular beam width. The black fit represents the experimental fit. Obtained data were normalized to the area under the curve.

3.2 EBT3 film measurements

3.3.1 Film Calibration

Fig 28 shows the optical density-to-dose calibration curve in terms of ADC values and the associated residual plot. As can be seen in the residual plot, the percentage deviations are really small and the uncertainty introduced due to the calibration can be neglected.

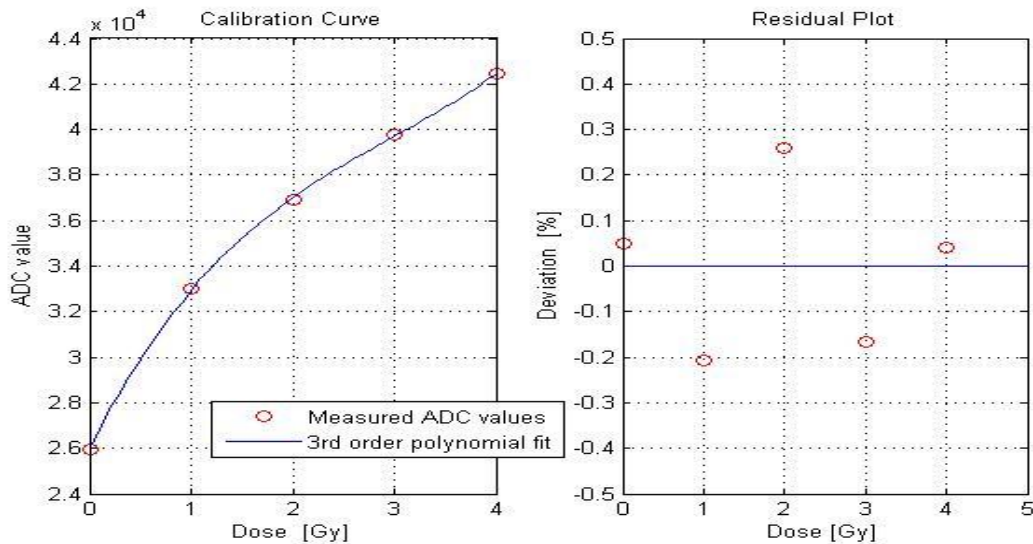


Figure 28: Calibration curve obtained for beam doses 1, 2, 3 and 4 Gy where a 3rd order polynomial fit generates the calibration curve. The percentage deviation between the fitted curve and measured ADC value can be seen in the right graph. The calibration curve was corrected for background.

3.3.2 Perturbed dose distributions

Dose distributions were measured with films downstream of the fiducial markers. The figures below show the dose distributions and the dose profiles at mid-SOBP and near the end of the SOBPs for each marker. All represented dose profiles were normalized to 100% in the regions not perturbed by the markers in order to facilitate the estimation of the dose perturbation (see Fig 20). The statistical uncertainty was calculated to $\pm 2\%$.

Markers localized at mid-SOBP

The perturbation in presence of the proton marker (0.6 mm x 4.0 mm) positioned perpendicular and parallel at mid-SOBP is shown in Figures 29 and 30. The maximum dose perturbation was found for the parallel oriented marker which caused an underdosage of $22\pm 2\%$. The maximal dose perturbation in presence of the perpendicular oriented proton marker was estimated to $11\pm 2\%$.

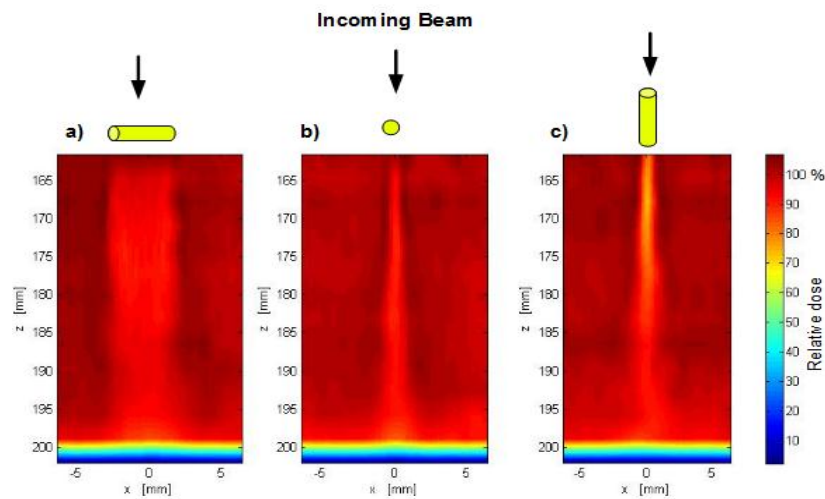


Figure 29: Dose perturbation downstream of the proton marker at depth $t_w = 162.5 \pm 0.3$ mm where the marker is oriented perpendicular (a and b) and parallel (c) to the beam axis at mid-SOBP. The dose is normalized to an unperturbed region.

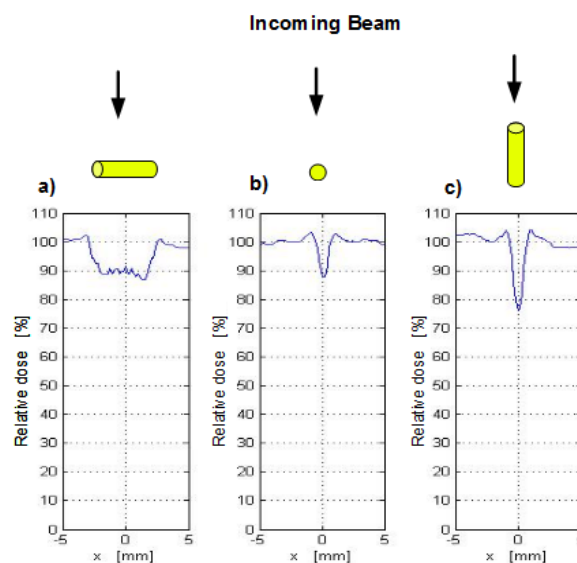


Figure 30: Lateral dose profiles at the maximum dose perturbation in Figure 29. The maximum dose perturbation occurred in case a) and b) at 8.1 ± 0.4 mm and in case c) at 2.0 ± 0.4 mm away from the downstream edge of the proton marker.

In Figure 31 and 32 the perturbation is shown in presence of the zigzag Gold Anchor marker (0.28 mm x 20.0 mm) positioned perpendicular and parallel at mid-SOBP. The maximum dose perturbation was found for the parallel oriented marker which caused an underdosage of $19\pm 2\%$. The maximum dose perturbation in presence of the perpendicular oriented proton marker was estimated to $4\pm 2\%$ which was the lowest dose perturbation measured in this work.

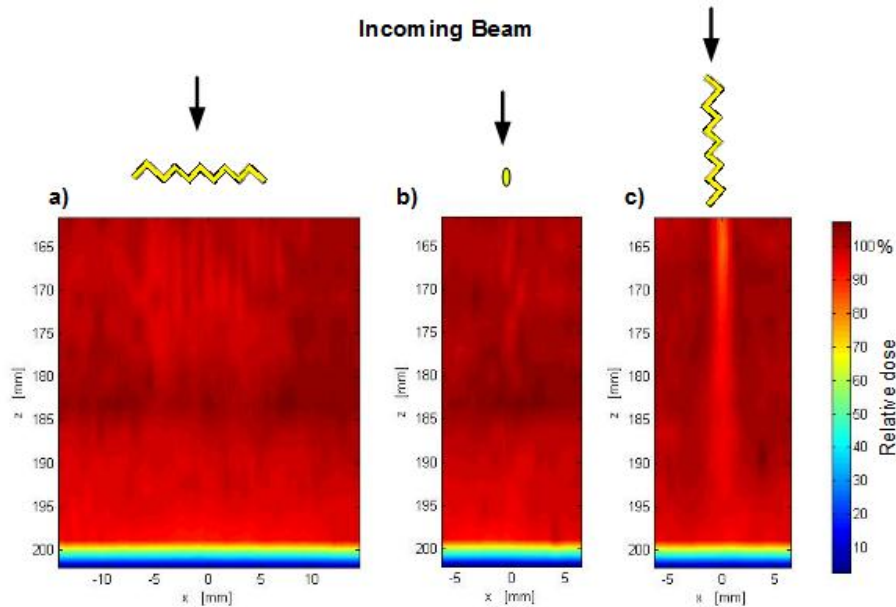


Figure 31: Dose perturbation downstream of the zigzag Gold Anchor marker at depth $t_w=161.6\pm 0.3$ mm with the marker oriented perpendicular (a and b) and parallel (c) to the beam axis at mid-SOBP. The dose is normalized to an unperturbed region.

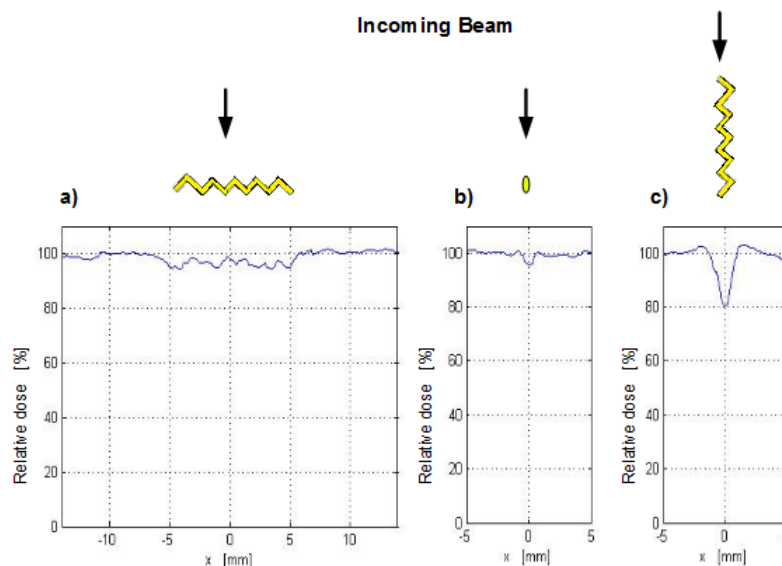


Figure 32: Lateral dose profiles at the maximum dose perturbation in Figure 31. The maximum dose perturbation occurred in case a) and b) at 10.7 ± 0.4 mm and in case c) at 3.8 ± 0.4 mm away from the downstream edge of the Gold Anchor marker.

Table 5 summarizes the maximum dose perturbation for the different markers at mid-SOBP and the distance (z_s) between the downstream edge of the marker and the maximal dose perturbation in terms of water-equivalent thickness.

Table 5: Summary of the maximum dose perturbation for each marker at mid-SOBP and the distance (z_s) along the depth between the downstream edge of the marker and the maximal dose perturbation in terms of water-equivalent thickness with the associated reading errors. The downstream edge of the proton marker was positioned at $t_w = 162.5 \pm 0.3$ mm SOBPs and the zigzag Gold Anchor marker was positioned at $t_w = 161.6 \pm 0.3$ mm SOBPs.

Marker	Orientation	$\% \Delta D_{\text{mean}}$	$\% \Delta D_{\text{max}}$	z_s
Zigzag Gold Anchor	Perpendicular	4±2 %	4±2 %	10.7±0.4mm
	Parallel	-	19±2 %	3.8±0.4mm
Proton	Perpendicular	11±2 %	12±2 %	8.1±0.4mm
	Parallel	-	22±2%	2.0±0.4mm

Markers localized near the end of the SOBP

The maximum dose perturbation for markers localized near the end of the SOBP was estimated in a 10 mm region (water-equivalent) downstream of the marker.

In Fig 32 and 33 the perturbation is shown in presence of the proton marker (0.6 mm x 4.0 mm) positioned perpendicular and parallel near the end of SOBP. The maximal dose perturbation was found for the parallel oriented marker which caused an underdosage of $49\pm 2\%$. The maximal dose perturbation in presence of the perpendicular oriented proton marker was estimated to $21\pm 2\%$.

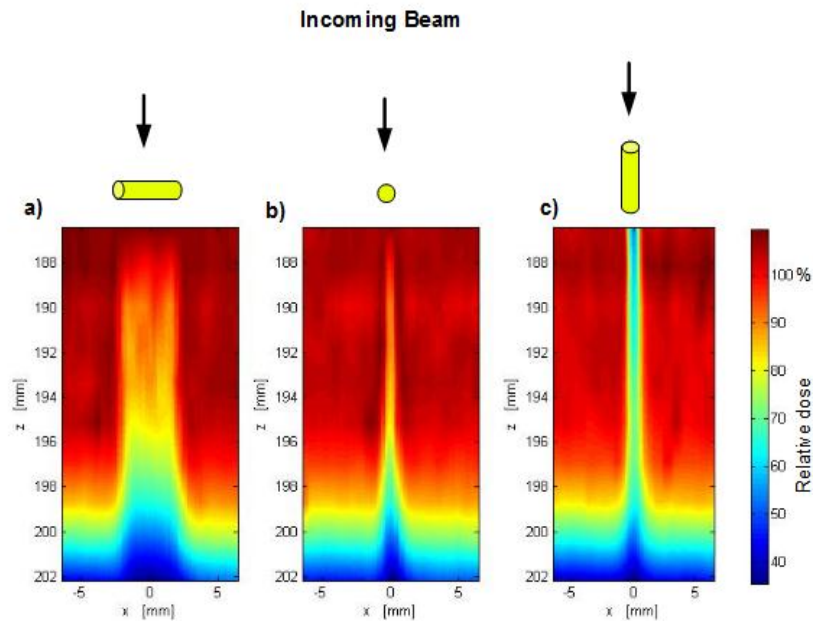


Figure 33: Dose perturbation downstream of the proton marker at depth $t_w=186.4\pm 0.3$ mm with the marker oriented perpendicular (a and b) and parallel (c) to the beam axis near the end of the SOBP. The dose is normalized to an unperturbed region.

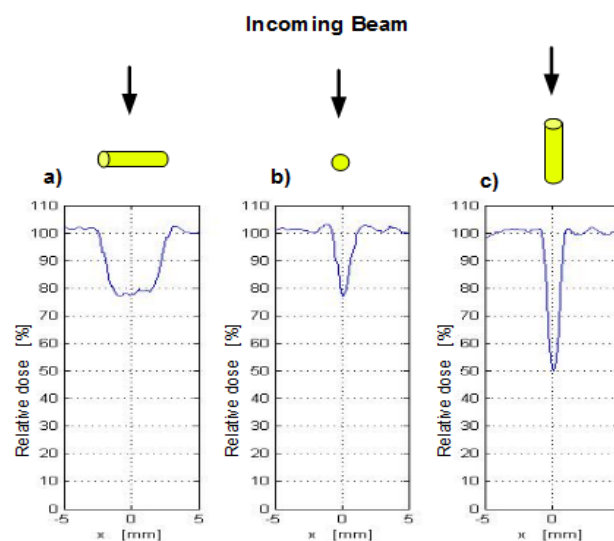


Figure 34: Lateral dose profiles at the maximum dose perturbation in Figure 33. The maximum dose perturbation occurred in case a) and b) at 8.9 ± 0.5 mm away from the downstream edge of proton marker and in case c) exactly behind the downstream edge of the proton marker.

Figures 35 and 36 show the dose perturbation in presence of the zigzag shaped Gold anchor marker (0.28 mm x 20.0 mm) near the end of SOBP. The marker oriented parallel to the beam axis caused a dose perturbation of $25\pm 2\%$. In the perpendicular oriented case the perturbation was estimated to $6\pm 2\%$ with a maximum perturbation of $9\pm 2\%$. As can be seen in Fig 35 a), there is a small problem in the alignment which may be due to small angulation of the phantom, discussed more in detail in section 4.

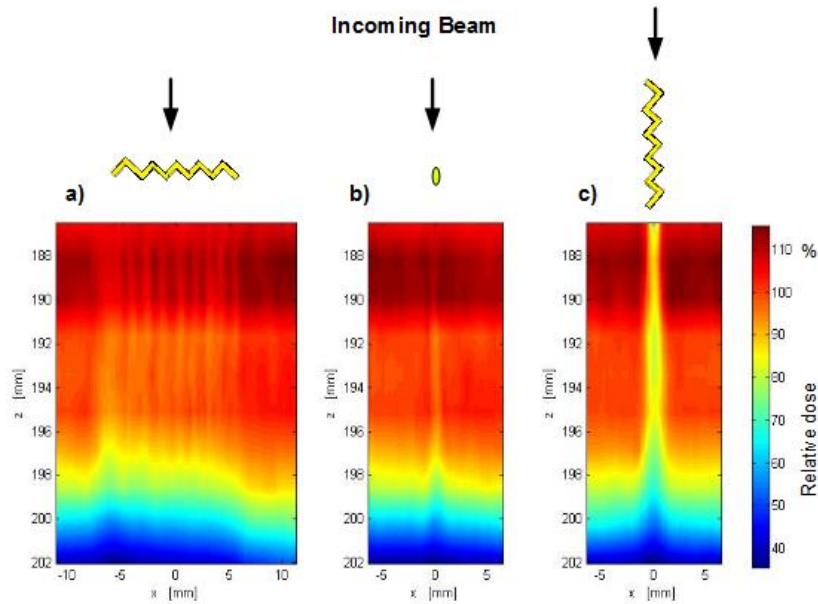


Figure 35: Dose perturbation downstream of the zigzag Gold Anchor marker at depth $t_w=186.5\pm 0.3$ mm with the marker oriented perpendicular (a and b) and parallel (c) to the beam axis near the end of the SOBP. The dose is normalized to an unperturbed region.

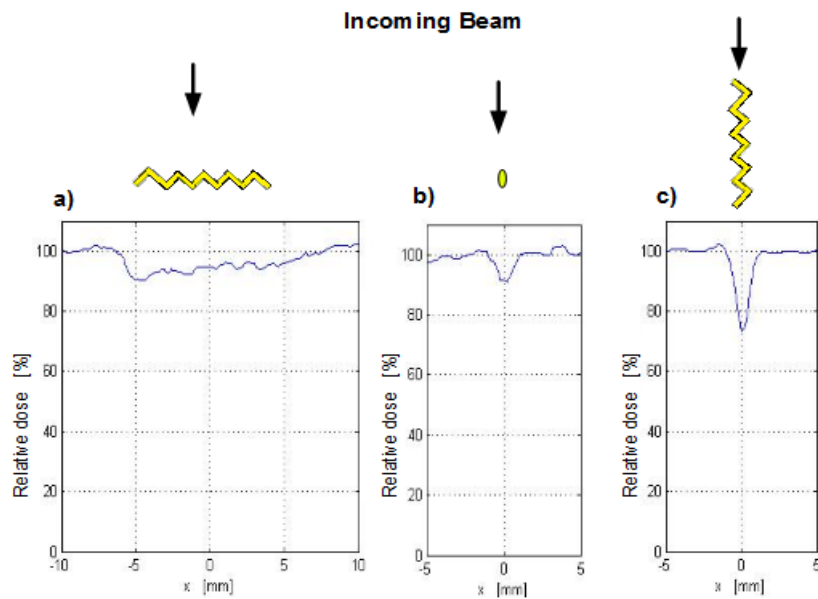


Figure 36: Lateral dose profiles at the maximum dose perturbation in Figure 35. The maximum dose perturbation occurred in case a) and b) at 8.9 ± 0.5 mm away from the downstream edge of the marker and in case c) exactly behind the downstream edge of the marker.

In Fig 37 the depth dose distributions are shown in presence of the curled Gold Anchor marker near the end of the SOBP. The dose profiles for the dose perturbation, about 6 mm away from the marker are shown in Fig 38 which caused an underdosage of $11\pm 2\%$. The maximum dose perturbation occurred at about 9 mm downstream from the distal edge of the marker causing a dose reduction of $21\pm 2\%$.

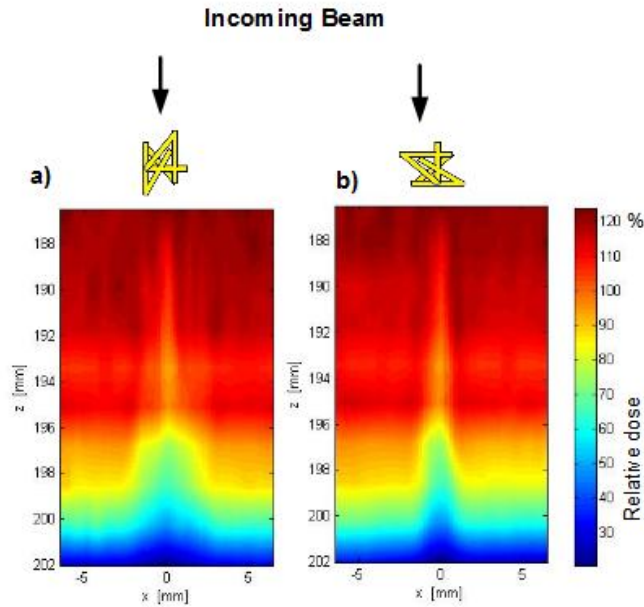


Figure 37: Dose perturbation downstream of the curled Gold Anchor marker at depth $t_w=186.5\pm 0.3$ mm in two orthogonal sections. The dose is normalized to an unperturbed region.

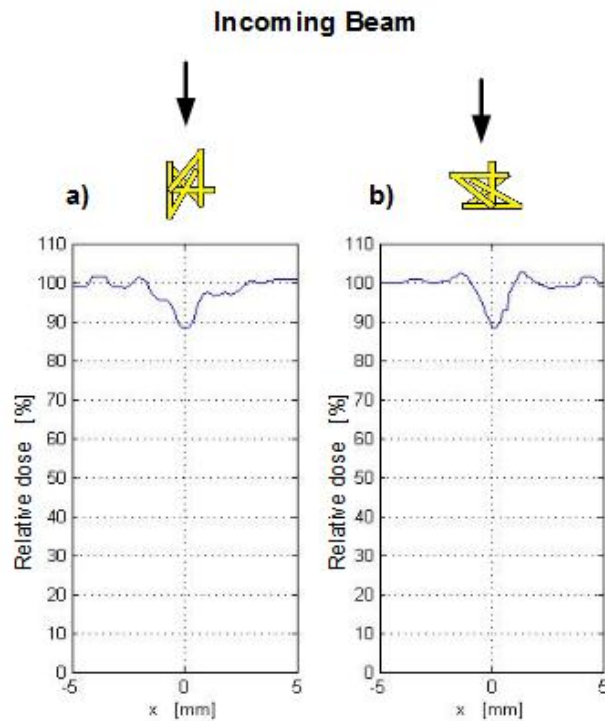


Figure 38: Lateral dose profiles at the dose perturbation at a depth of 192.5 mm. The dose perturbation occurred 6.0 ± 0.4 mm away from the downstream edge of the curled Gold Anchor marker.

In Fig 39 the dose perturbation is shown in presence of the photon marker (1.2 x 3.0 mm) near the end of the SOBP. The photon marker which was the thickest marker caused as expected large dose reductions. The maximum dose perturbation is shown in Fig 40. The parallel oriented marker reduced the dose up to $85\pm 2\%$ while the perpendicular oriented photon marker resulted in an underdosage of almost 60%

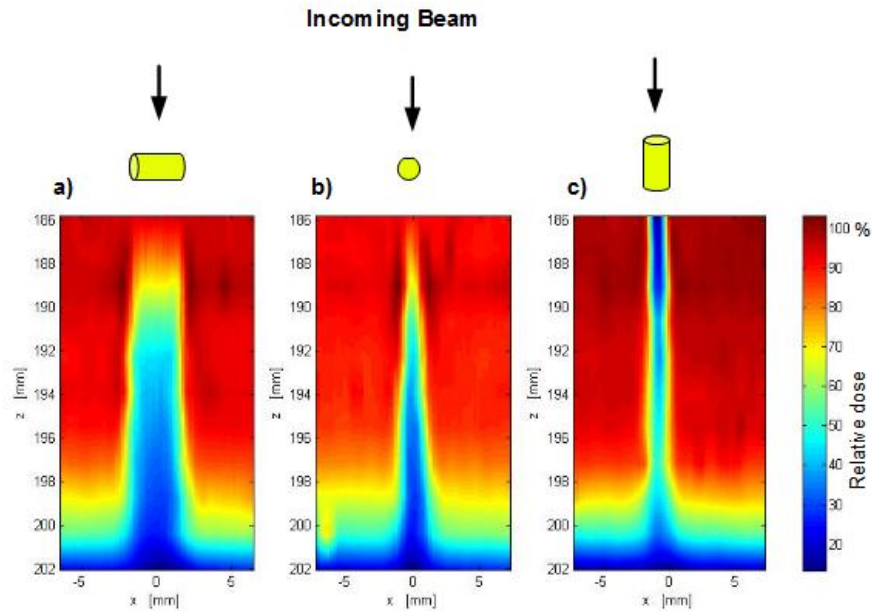


Figure 39: Dose perturbation downstream of the photon marker at depth $t_w=185.8\pm 0.3$ mm with the marker oriented perpendicular (a and b) and parallel (c) to the beam axis near the end of the SOBP. The dose is normalized to an unperturbed region.

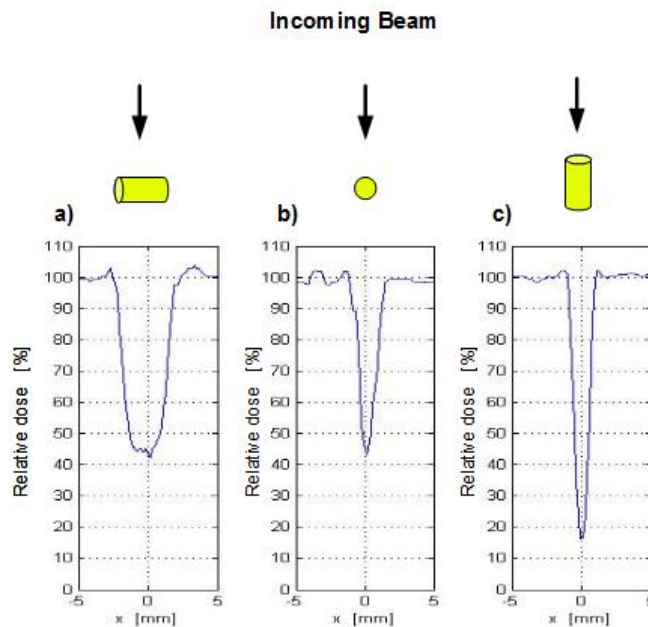


Figure 40: Lateral dose profiles at the maximum dose perturbation in Figure 39. The maximum dose perturbation occurred in case a) and b) at 8.6 ± 0.5 mm away from the downstream edge of the marker and in case c) exactly behind the downstream edge of the photon marker.

Table 6 summarizes the maximum dose perturbation for the different markers near the end of the SOBP and the distance (z_s) between the downstream edge of the marker and the maximal dose perturbation in terms of water-equivalent thickness.

Table 6: Summary of the maximum dose perturbation for each marker near the end of the SOBP and the distance (z_s) along the depth between the downstream edge of the marker and the maximal dose perturbation in terms of water-equivalent thickness with the associated reading errors.

Marker	Orientation	%ΔD_{mean}	%ΔD_{max}	z_s
Proton	Perpendicular	21±2%	22±2%	8.8 ± 0.5 mm
	Parallel	-	49±2%	0 mm
Zigzag Gold Anchor	Perpendicular	6±2 %	9±2 %	8.9 ± 0.5mm
	Parallel	-	25±2 %	0 mm
Curled Gold Anchor	Curled	-	21±2%	8.9 ± 0.5mm
Photon	Perpendicular	58±2 %	59±2 %	8.6 ± 0.5mm
	Parallel	-	85±2 %	0 mm

3.3 Geant4 estimation of the disturbed dose distribution

The dose distribution in presence of the proton marker near the end of the SOBP was calculated with Geant4 simulations. The dose distributions are shown in Figure 41 and the maximum dose perturbation can be seen in Figure 42. The simulations were performed by using a PMMA phantom with a voxel size of $0.5 \times 0.5 \times 1.0 \text{ mm}^3$ where the dose was scored in the middle of each voxel. This means that one voxel, along the depth, corresponds to 1.16 mm water. The voxel size was chosen to get reasonable statistics. The spatial resolution was therefore much cruder than in the experiment. The statistical fluctuation was estimated to $\pm 3\%$.

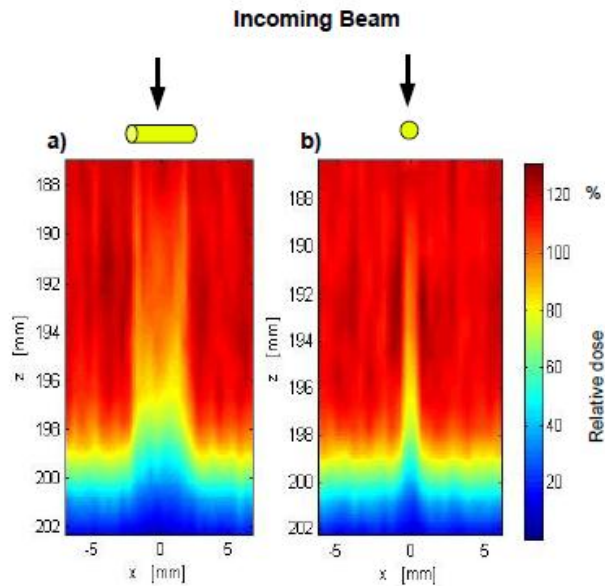


Figure 41: Dose perturbation calculated with Geant4 downstream of the proton marker at depth $t_w = 186.4 \pm 0.3 \text{ mm}$ with the marker oriented perpendicular (a and b) to the beam axis near the end of the SOBP. The dose is normalized to an unperturbed.

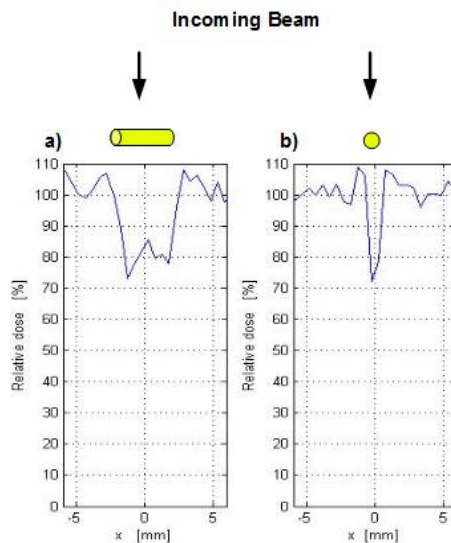


Figure 42: Lateral dose profiles at maximum dose perturbation calculated with Geant 4 for the proton marker positioned near the end of the SOBP. The dose perturbation was determined to $19 \pm 3\%$ and $24 \pm 3\%$, respectively. The maximum dose perturbation occurred at around 9.3 mm downstream of the marker.

3.4 Comparison of experimental data with MC-calculations

Direct comparisons between film measurements and MC simulations are presented in Figures 43, 44 and in Table 6. Figure 43 shows the calculated unperturbed depth dose distribution together with the calculated and measured perturbed dose distributions from the proton marker. A marked reduction in proton range can be seen (cf Fig 39 and 41). The agreement between calculation and experiment is relatively good. Figure 44 shows calculated and experimental dose profiles at three different depths. Also here the agreement is good. Table 6 summarises the calculated and measured maximum dose perturbations at different depths.

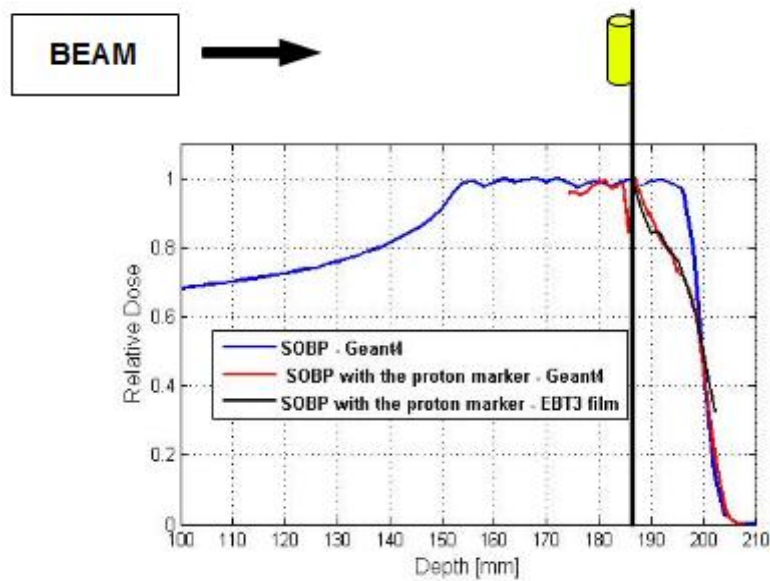


Figure 43: Calculated dose perturbation with Geant4 (red curve) and film measurement (black curve), and the unperturbed SOBP with Geant4 (blue curve). Note that, the dose drop down (black curve) at the region behind the marker (near the end of the range) is missing. This is due to no measured points in that region. However, this is of less of concern, as the dose perturbation in a region of around 10 mm away from the downstream edge of the marker was of interest.

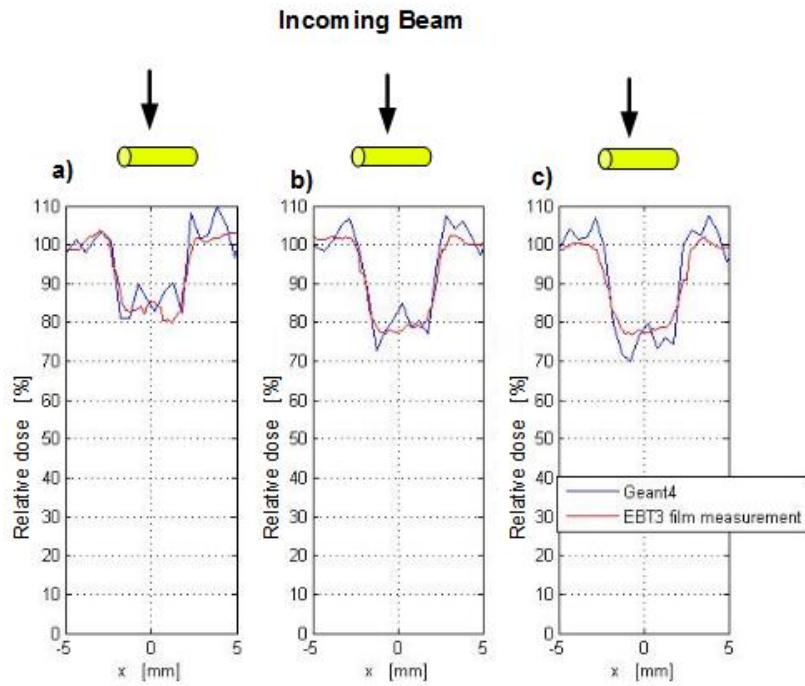


Figure 44: Relative dose perturbations in presence of the perpendicular oriented proton marker, calculated with Geant4 and EBT3 films at nearest corresponding depths in the SOBP given in Table 7.

Table 7: Summary of dose perturbations associated with Figure 44 and the distance along the depth (z_s) between the downstream edge of the marker and the dose perturbation in terms of water-equivalent thickness for the three cases.

	Case a)		Case b)		Case c)	
	EBT3	Geant4	EBT3	Geant4	EBT3	Geant4
Dose reduction	$18 \pm 2\%$	$13 \pm 3\%$	$21 \pm 2\%$	$19 \pm 3\%$	$21 \pm 2\%$	$22 \pm 3\%$
z_s	6.0 ± 0.5 mm	5.8 ± 0.6 mm	8.8 ± 0.5 mm	9.3 ± 0.6 mm	10.3 ± 0.6 mm	10.4 ± 0.6 mm

4. DISCUSSION

4.1 Adjustment of the Geant4 dose distribution and comparison with experimental diode measurements

Comparison of the dose distribution of Geant4 simulation was performed with diode measurements in the nearly monoenergetic beam and in the modulated beam. An adjustment of the initial beam energy of the unmodulated beam to of 178.3 ± 0.2 MeV resulted in good agreement with the experiment. The differences between the curves are probably caused by the fact that the whole beam line was not modelled in MC. In addition, in the area of hadronic interactions of charged particles at energies in the order of a few MeV, especially for low Z materials, there is no physics model able to reproduce the experimental data. For this reason, in the default version of Geant4, the cross sections and the production of secondary particles in proton-nucleus interactions for energies below 20 MeV is not accurate. However, for the SOBP comparison (RM width = 48 mm) these differences are smoothed out resulting in small differences which can be seen in Figure 25.

The effect of the differences in the modelled MC beam line is most pronounced for the unmodulated lateral dose profiles especially at the edges, shown in Figure 24. However, this is of less concern as the markers in the film measurements were placed in the central part with homogenous dose.

4.2 Estimation of the impact of the initial beam size and initial spread

The impact of initial beam size and spread in water was determined by varying the initial beam parameters such as the initial radial and angular Gaussian distributions by examining the penumbras obtained with a collimator aperture of 40 mm. As can be seen in Figures 26 and 27 the penumbras are almost identical regardless of initial beam size and angular spread. This means that the impact of the initial beam size and beam spread is negligible.

4.3 EBT3 film measurements

EBT3 film measurements showed that all investigated markers reduced the target dose in small volumes. The effect was most pronounced for markers oriented parallel to the beam axis and increased near the end of the SOBP. For example, the maximum dose reduction in presence of the parallel oriented proton marker at mid-SOBP is 22% and a change of the localization to the end-SOBP resulted in a maximum dose reduction of almost 50%. As expected, the effect was also depending on the material thickness of the marker. The photon marker, which was the thickest marker used in this work, caused an underdosage up to 85% near the end of the SOBP.

Investigation of Fig 35 shows a small alignment problem. The left edge of the marker seems to be a little bit closer to the end of the SOBP which can also be seen in Fig 36. This may cause a higher dose reduction at the left edge. On the other hand, the right edge of the beam gives smaller dose perturbation which will then be smoothed out and may not have a major impact on $\% \Delta D_{\text{mean}}$. However, $\% \Delta D_{\text{max}}$ estimated for the perpendicular oriented zigzag marker may in this case be overestimated.

The underdosage is explained by the underlying physical processes, discussed also in section 1.2.3. The protons that pass through the marker underwent more scattering than those that did not, causing a laterally fluence disequilibrium [15] and the energy decreases due to the energy absorption in the high density material of the marker. This causes also a range-shift effect, which is most pronounced for markers placed near the end of the SOBP where the energy of the protons is relatively low.

Comparison of the dosimetric perturbations between the Gold Anchor marker and the proton marker, used today at TSL, shows a reduced underdosage with the Gold Anchor marker. The maximum dose shadow for the zigzag shaped Gold Anchor at mid-SOBP, which is a typical implantation depth, was $4\pm 2\%$ for perpendicular orientation and $19\pm 2\%$ for the parallel orientation. For the same orientations and placement, the dose perturbations for the proton marker were $12\pm 2\%$ and $22\pm 2\%$. As can be seen in table 5 and 6, it is clear that of all the investigated markers the Gold Anchor marker causes the least dose perturbations in proton beams.

The uncertainty analysis in the film experiment was performed by estimating type A uncertainties. The type B uncertainties were neglected due to difficulties in the estimation. The introduced calibration uncertainty was also neglected due to the small deviations which can be seen in Fig 28. Type B uncertainty which could be introduced in the scanning process such as the scanning orientation was taken into account. Another influencing factor was the film-to-film variations and the differences on the optical density in the film. However, these differences are of less concern in relative dose estimations.

4.4 Comparison of experimental data with MC-calculations

The MC simulations showed that the proton marker reduced the target dose up to $19\pm 3\%$ near the end of the SOBP, which can be seen in Figures 41 and 42. The type A uncertainty was estimated with the batch method to 3%. The statistical uncertainty depends on the size of the voxel and the number of histories. More histories and larger voxel size decreases the magnitude of the type A uncertainty.

As can be seen in fig 42 and 44, there is a large discontinuity in Geant4 dose profiles which depends mainly on the dose calculation in Geant4. The dose is calculated at the middle of the voxels. As the voxel size was $0.5\times 0.5\times 1.0\text{ mm}^3$, this may influence the Geant4 dose calculations. However, larger voxel size gives better statistics and this influence may be negligible as the mean value of the maximum dose perturbation is estimated.

Fig 43 and 44 show good agreement between the film measurements and the MC calculations. The observed dose shadows in both methods agreed within their respective statistical uncertainties. The most noticeable difference was seen in Figure 44 a) (see also Table 7). The dose perturbation was calculated to $18\pm 2\%$ for the film measurement and $13\pm 3\%$ for MC measurements. Other influencing factors on the result which were not taken into account may be;

- 1- The material of the MC phantom (only PMMA instead of PMMA and film)
- 2- The MC beam line was a simplified version of the beam line at TSL
- 3- The Geant4 cross sections and the production of secondary particles in proton-nucleus interactions for energies below 20 MeV is not accurate
- 4- Type B uncertainties and errors in the film measurements were neglected

However, the dose perturbation was almost of the same magnitude and the deviation between the film measurement and MC calculations was generally within $\pm 5\%$.

5. CONCLUSION

Radiopaque fiducial markers give dose perturbations in small volumes in all investigated cases. The magnitude of the perturbation depends on the shape, thickness, orientation and localization of the markers. The effect was most pronounced for markers oriented parallel to the beam axis and increased close to the distal end of the SOBP. The maximum dose perturbation for the zigzag shaped Gold Anchor at mid-SOBP, which is a typical implantation depth, was $4\pm 2\%$ for perpendicular orientation and $19\pm 2\%$ for the parallel orientation. For the same orientations and placement, the dose perturbations for the proton marker were $12\pm 2\%$ and $22\pm 2\%$. As the perturbation increases with the thickness of the marker, the photon marker caused the maximum dose perturbation in this work.

The proton marker, oriented perpendicular to the beam axis near the end of the SOBP gave a dose perturbation of $21\pm 3\%$ with film measurements and $19\pm 3\%$ with MC simulations. The MC simulations agreed generally well with the film measurements and the maximum deviation was within $\pm 5\%$.

In a clinical situation it is common that beams are delivered from different directions and that the organs move somewhat during fractions or between fractions, which means that the underdosage to some extent will be levelled out. A normal prostate gland size is about $25\text{-}30\text{cm}^3$ [44] and the size of the prostate gland increases with age. Usually 3-4 markers are implanted in the prostate. For a proton marker at mid-SOBP, oriented perpendicular to beam axis, the dose is reduced up to 11%. Thereby, the dose is reduced to approximately 5% in a range of around 30 mm along the depth. This corresponds to a volume of around 0.07 cm^3 ($0.6\times 4.0\times 30\text{ mm}^3$). For example, if there are four proton markers implanted in the prostate, the underdosage volume in the prostate gland will correspond to around 1% of the total volume. This means that the dose perturbation when the marker is oriented perpendicular to the beam axis at mid-SOBP can be neglected. However, localization and orientation of the marker has an major impact. For example, when the proton marker was oriented parallel to the beam axis and localized near the end of SOBP, the dose perturbation was much larger which may have a negative influencing effect on the tumour cell kill process (e.g the dose reduction was almost 50% near the end SOBP).

Of the investigated markers the Gold Anchor marker causes the least dose perturbations in proton beams. Furthermore, Naslund Medical AB offers also Gold Anchor markers with a length of 10 mm. This marker would in the case of parallel orientations reduce the dose perturbation by half.

Thus, the major advantages of the Gold Anchor marker makes it superior and may be used in future PBT.

6. REFERENCES

1. O. Bergman, L. Jacobson, M. Jaresand, *Cancerfondsrapporten*, Stockholm, 2013
<http://www.cancerfonden.se/Documents/cfr13/cancerfondsrapporten2013.pdf>
2. National Cancer Institute, *Radiation Therapy for Cancer*, United States, 2010
<http://www.cancer.gov/cancertopics/factsheet/Therapy/radiation>
3. J Wickström, *Strålning kan både bota och skada*, SSM, Stockholm, 2011
<https://www.stralsakerhetsmyndigheten.se/Om-myndigheten/Tema-stralsakerhet/Stralsakerter/Artiklar/Stralning-kan-bade-bota-och-skada/>
4. PTCOG, *Particle therapy facilities in operation*, 2013
<http://ptcog.web.psi.ch/ptcentres.html>
5. PTCOG, *Particle therapy facilities in a planning stage or under construction*, 2013
<http://ptcog.web.psi.ch/newptcentres.html>
6. W. P. Levin, H. Kooy, J. S. Loeffler and T. F. DeLaney, *Proton Beam Therapy*, British Journal of Cancer, vol. 93, No 8, pp 849–854, 2005
7. W. Newhauser, J. Fontenot, N. Koch, L. Dong, A. Lee, Y. Zheng, L. Waters and R. Mohan, *Monte Carlo simulations of the dosimetric impact of radiopaque fiducial markers for proton radiotherapy of the prostate*, Physics in Medicine and Biology, Vol 52, No 11, pp 2937–2952, 2007
8. J. Apostolakis, M. Asai, G. Cosmo, A. Howard, V. Ivanchenko, M. Verderi, *Parallel Geometries in Geant4: foundation and recent enhancements*, Proceedings of the 2008 IEEE NSS/MIC/RTSD Conference, 2008
9. Paganetti H., *Proton Therapy Physics*, Series in Medical Physics and Biomedical Engineering, Massachusetts General Hospital, 2012
10. D.T.L. Jones, *Reference dosimetry for fast neutron and proton therapy*, Radiochimica Acta 89, pp 279-287, 2001
11. *History of Proton Therapy*, Optivus Proton Therapy, Inc., Loma Linda, California, 2008
<http://hstrial-optivusprotonthe.homestead.com/~local/~Preview/historypbt.pdf>
12. Synthesis, *History of proton beam therapy*, UC Davis Cancer Center, Sacramento, 2006
http://www.ucdmc.ucdavis.edu/synthesis/issues/fall_winter_06-07/features/history.html
13. E. Pedroni ,R. Bacher, H. Blattmann, T. Böhringer, A. Coray, A. Lomax, S. Lin, G. Munkel, S. Scheib, U. Schneider, A.Tourovsky. *The 200-MeV proton therapy project at the Paul Scherrer Institute: conceptual design and practical realization*. Medical Physics , vol 22, pp 37-53, 1995

14. T. Kanai, K. Kawachi, Y. Kumamoto, H. Ogawa, T. Yamada, H. Matsuzawa, T. Inada, *Spot scanning system for proton radiotherapy*. Medical Physics, vol 7, no 365-369, 1980
15. M. Goitein, *Radiation Oncology: A Physicist's-Eye View*, © Springer, Harvard Medical School, 2008
16. W. D. Newhauser, N. C. Koch, J. D. Fontenot, S. J. Rosenthal, D. S. Gombos, M. M. Fitzek and R. Mohan, *Dosimetric impact of tantalum markers used in the treatment of uveal melanoma with proton beam therapy*, Physics in Medicine and Biology, vol 7, no 52, pp 3979-90, 2007
17. ICRU, *Prescribing, recording, and reporting photon beam therapy*, In ICRU report. Volume 50, Bethesda: International Commission on Radiation Units and Measurements, 1993
18. K.R. Britton, Y. Takai, M Mitsuya, K. Nemoto, Y. Ogawa and S. Yamada, *Evaluation of inter- and intrafraction organ motion during intensity modulated radiation therapy (IMRT) for localized prostate cancer measured by a newly developed on-board image-guided system*, Radiation Medicine, Vol. 23 No. 1, pp 14–24, 2005
19. D. Verellen, M. D. Ridder, N. Linthout, K. Tournel, G. Soete and G. Storme, *Innovations in image-guided radiation therapy*, Nature Publishing Group, vol 7, no 12, pp 949-960, 2007
20. L.L. Handsfield, N. J. Yue, J. Zhou, T. Chen, S. Goyal, *Determination of optimal fiducial marker across image-guided radiation therapy (IGRT) modalities: visibility and artifact analysis of gold, carbon, and polymer fiducial markers*, Journal of applied clinical medical physics, vol 13, no 5, 2012
21. D. Habermehl, K. Henhner, S. Ecker, O. Jäkel, J. Debus, S. E. Combs, *Evaluation of different fiducial markers for image-guided radiotherapy and particle therapy*, Journal of Radiation Research, vol 54, pp i61–i68, 2013
22. Y. K. Lim, J. Kwak, D. W. Kim, D. Shin, M. Yoon, S. Park, J. S. Kim, S. H. Ahn, J. Shin, S. B. Lee, S. Y. Park, H. R. Pyo, D. Y. Kim and K. H. Cho, *Microscopic gold particle-based, fiducial markers for proton therapy of prostate cancer*, International Journal of Radiation Oncology, Biology, Physics, vol. 74, No. 5, pp. 1609–1616, 2009
23. E. B. Podgorsak (Ed.), *Radiation Oncology Physics: A Handbook for Teachers and Students*, International Atomic Energy Agency, Vienna, 2005
24. S. Devic, *Radiochromic film dosimetry: Past, present and future*, Physica Medica, vol 27, no 3, pp 122-134, 2011
25. V.C Borca, M. Pasquino, G. Russo, P. Grosso, D. Cante, P. Sciacero, G. Girelli, M. R. L. Porta, S. Tofani, *Dosimetric characterization and use of GAFCHROMIC EBT3 film for IMRT dose verification*, Journal of applied clinical medical physics, vol 14, no 2, 2013
26. S. Reinhardt, M. Hillbrand, J. J. Wilkens, W. Assmann, *Comparison of Gafchromic EBT2 and EBT3 films for clinical photon and proton beams*, Medical Physics, vol 39, no 8, August 2012

27. A. Niroomand-Rad, C. R. Blackwell, B. M. Coursey, K. P. Gall, J. M. Galvin, W. L. McLaughlin, A. S. Meigooni, R. Nath, J. E. Rodgers, C. G. Soares, *Radiochromic film dosimetry. Recommendations of AAPM Radiation Therapy Committee Task Group 55*, Medical Physics, vol 25, no 11, pp 2093–2115, 1998
28. J. T. Bushberg, J. A. Seibert, E. M. Leidholdt, and J. M. Boone, *The Essential Physics of Medical Imaging*, Lippincott Williams & Wilkins, 2nd edition, 2002
29. S. Agostinelli, J. Allison, K. Amako, J. Apostolakis, H. Araujo, *Geant4: A simulation toolkit*, Nuclear Instruments and Methods in Physics Research Section A, vol. 506, no. 3, pp. 250–303, 2003
30. J. Allison, K. Amako, J. Apostolakis, H. Araujo, P. Arce Dubois, *Geant4 developments and applications*. IEEE Transactions on Nuclear Science ., vol 53, no 1, pp 270-278, 2006
31. J. Schumann, J. Shin , B. A. Faddegon, H. Paganetti, J. Perl, *Efficient voxel navigation for proton therapy dose calculation in TOPAS and GEANT4*, Physics in Medicine and Biology, vol 57, no 11, pp 3281-93, 2012
32. S. Enger, G. Landry, M. D'Amours, F Verhaegen, L Beaulieu, M Asai, J Perl, *Layered mass geometry: a novel technique to overlay seeds and applicators onto patient geometry in Geant4 brachytherapy simulations*, Physics in Medicine and Biology, vol 57, no 19, pp 6269-6277, 2012
33. Geant4 User's Guide for Application Developers, *Chapter 3. Toolkit Fundamentals*, <http://geant4.web.cern.ch/geant4/UserDocumentation/UsersGuides/ForApplicationDeveloper/html/ch03.html>
34. L. Rädcl, *Simulation Studies of the Cherenkov Light Yield from Relativistic Particles in High Energy Neutrino Telescopes with Geant4*, Master's Thesis, der Rheinisch-Westfälischen Technischen Hochschule, Aachen, September 2012
35. Geant4, *Reference physics lists*, http://geant4.cern.ch/support/proc_mod_catalog/physics_lists/referencePL.shtml
36. A.V. Ivantchenko, V. N. Ivanchenko, J. M. Q. Molina, S. L. Incerti, *Geant4 hadronic physics for space radiation environment*, International Journal of Radiation Biology, vol 88, no 1-2, pp 171-175, 2012
37. Geant4, *Physics reference Manual*, Version: geant4 9.5.0 , 2011 <http://geant4.web.cern.ch/geant4/UserDocumentation/UsersGuides/PhysicsReferenceManual/BackupVersions/V9.5/fo/PhysicsReferenceManual.pdf>
38. A. Ribon, J. Apostolakis, A. Dotti, G. Folger, V. Ivanchenko, M. Kosov, V. Uzhinsky , D. H. Wright, *Status of Geant4 hadronic physics for the simulation of LHC experiments at the start of LHC physics program*, CERN-LCGAPP-2010-02, Version 1.0, 2010
39. E. Grusell, A. Montelius, A. Brahme, G. Rikner, K. Russell, *A general solution to charged particle beam flattening using an optimized dual-scattering-foil technique, with application to proton therapy beams*, Physics in Medicine and Biology, vol 39, pp 2201-2216, 1994
40. E. Bäckmann, *Dose contribution from δ -electrons in proton radiotherapy*, <http://medim.sth.kth.se/hl2009/ElanorBackman.pdf>

41. U. Titt, D. Mirkovic, G. O. Sawakuchi, L. A. Perles, W. D. Newhauser, P. J. Taddei, R. Mohan, *Adjustment of the lateral and longitudinal size of scanned proton beam spots using a pre-absorber to optimize penumbrae and delivery efficiency*, *Physics in Medicine and Biology*, vol 55, no 23, pp 7097-7106, 2010
42. R. Grant, P. Summers, J. Neihart, A. Blatnica, N. Sahoo, M. Gillin, D. Followill, G. Ibbott, *Relative stopping power measurements to aid in the design of anthropomorphic phantoms for proton radiotherapy*, *Journal of applied clinical medical physics*, vol 15, no 2, 2014
43. P. Andreo, D. T. Burns, D. T. K. Hohlfeld, M. S. Huq, T. Kanai, F. Laitano, F. V. G. Smith and S. Vynckier, *Absorbed dose determination in external beam radiotherapy: an international Code of Practice for dosimetry based on standards of absorbed dose to water IAEA Technical Report Series No 398*, Vienna: International Atomic Energy Agency, 2000
44. A. V. D'amico, C. M. Tempany, R. Cormack, N. Hata, M. Jinzaki, K. Tuncali, M. Wienstein, J. P. Richie, *Transperineal magnetic resonance image guided prostate biopsy*, *The Journal of Urology*, vol 164, no 2, pp 385-387, 2000